Vertical structure and temporal variability of currents over the Chukchi Sea continental slope

Phyllis J. Stabeno[a,*], Ryan M. McCabe[b]

[a]*NOAA Pacific Marine Environmental Laboratory (PMEL), Ocean Environment Research Division, 7600 Sand Point Way NE, Seattle, WA 98115-6349*
[b]*Joint Institute for the Study of the Atmosphere and Ocean (JISAO), University of Washington, 3737 Brooklyn Ave NE, Seattle, WA 98195*.

[*]Corresponding author.
E-mail address: phyllis.stabeno@noaa.gov (P.J. Stabeno)

Key Points

1) Three years of moored current and water property data confirm a well-defined, persistent westward surface-intensified flow along the northern Chukchi continental slope, called the Chukchi Slope Current.

2) The westward surface current extends to a depth of 200–250 m, depending on the year, and is strongest in the ice-limited summer season, and weaker during winter.

3) An eastward flowing undercurrent is evident below the surface current, spanning depths of ~300–800 m occupied by relatively warm Atlantic Water that is also enhanced during summer.

4) Fluctuations in currents and subsurface temperature are not correlated to local wind forcing, including wind stress curl.

5) We hypothesize that the fact that the Chukchi Slope Current flows northwestward along the continental slope is a consequence of dynamics associated with the Beaufort Gyre.

ABSTRCT

Observations from a single mooring site on the northern Chukchi Sea continental slope near the 1000-m isobath are presented. This site was occupied consecutively for three years (spanning September 2014 – August 2017). Vertically the flow divides into three depth ranges, the upper ~200 m, ~200 to ~850 m and near-bottom flow. In the upper ~200 m, the mean flow was northwestward and strongest in the summer months. During winter months, currents decreased in magnitude, and in some years even reversed in direction. Satellite-tracked drifter trajectories (drogue depth ~30 m) show this along-slope flow persists at least from 156 to 165 °W, with average velocity of ~17 cm s^{-1}. This northwestward flowing current is the Chukchi Slope Current. From ~250 m to ~850 m, the flow reversed; this weak flow is the Arctic-wide cyclonic boundary current advecting Atlantic Water. The mean flow at ~900 m is weak and on an annual time scale not significantly different from 0 cm s^{-1}. It consists of Arctic deep water. In the upper two layers, currents vary on the scale of days to seasons, with short-term reversals common. Currents below 40 m were not significantly correlated with local winds nor wind stress curl. We hypothesize that the fact that the Chukchi Slope Current flows northwestward along the continental slope is a consequence of dynamics associated with the Beaufort Gyre.

1. Introduction

The Chukchi Sea consists of a broad shallow (<80 m) shelf, extending >800 km northward from its southern boundary at Bering Strait to the shelf break bounding the Arctic basin (Fig. 1). Approximately 1×10^6 m^3 s^{-1} (1 Sverdrup [Sv]) of Pacific water enters the shelf through Bering Strait (Woodgate et al., 2005a, 2012) and continues generally northward following the bathymetry (Woodgate et al., 2005b). Most of this flow exits the Chukchi Shelf through two canyons—Barrow Canyon in the east (Coachman et al., 1975; Weingartner et al., 2005) and Herald Canyon in the west (Coachman et al., 1975; Pickart et al., 2010). The flow exiting via Barrow Canyon is a combination of the northward flow through Central Channel that joins the coastal flow offshore of Icy Cape. Exiting Herald Canyon, there is a relatively narrow eastward flowing shelfbreak jet (Linders et al., 2017; Corlett and Pickart, 2017; Li et al., 2019).

As Pacific water transits the Chukchi Shelf northward, it is modified through local physical and biological processes. In summer, when sea-ice coverage is marginal or absent, water over the shallow Chukchi Shelf gains heat. A portion of this excess summer heat is advected north from the Bering Sea through Bering Strait (e.g., Woodgate et al., 2012), but the heat gained locally over the Chukchi Shelf through solar radiation can also be substantial (Tsukada et al., 2018). The modified shelf water then flows off the shelf and into the Canada Basin (Shimada et al., 2001; Steele et al., 2004; Watanabe et al., 2017; Fine et al. 2018) where it contributes to the observed accumulation of heat (Timmermans et al., 2014, 2018). Excess subsurface heat, as far west as the Chukchi Abyssal Plain (just to the west of the Chukchi Borderland), was recently identified to have a Pacific origin (Watanabe et al., 2017). Such subsurface heat anomalies can persist for years (Watanabe et al., 2017; Fine et al. 2018) and

likely lead to delays in winter freeze-up and an overall decline of sea ice (Steele et al., 2008; Jackson et al., 2012; Timmermans, 2015; Serreze et al., 2016). The pathways of Pacific Water after exiting Barrow Canyon are not well known.

The basin in the vicinity of the Chukchi and Beaufort shelves is influenced by the anti-cyclonic Beaufort Gyre (Aagaard and Carmack, 1989; Regan et al., 2019), which dominates surface flow in the Canada Basin. Along the slope and beneath the Beaufort Gyre is the Arctic Ocean Boundary Current (AOBC; Woodgate et al., 2001), which moves Atlantic water cyclonically around the Arctic basin. The westward flowing Chukchi Slope Current (CSC) resides along the slope from Barrow Canyon to Herald Canyon (Corlett and Pickart, 2017; Stabeno et al., 2018; Li et al., 2019). The recently identified CSC appears to vary seasonally, with the strongest flow in the summer months and weak or even eastward flow dominating in the winter months. From earlier results, it appears to be confined to the upper ~300 m, with an eastward reversal at deeper depths (Stabeno et al., 2018). Analysis by Corlett and Pickart (2017) indicates that it is baroclinically unstable and meanders along the slope. Satellite-tracked drifter trajectories show that the CSC extends from at least Barrow Canyon to near Herald Canyon (Stabeno et al., 2018). Watanabe et al. (2017) used observations and a high-resolution numerical ocean model to demonstrate that Pacific-origin heat gets transported in the CSC as far west as the Chukchi Borderland.

This paper concentrates on a 34-month time series of currents, temperature and salinity collected at a single mooring site on the Chukchi continental slope. A single mooring was deployed in each of three years (2014, 2015 and 2016) in the late summer, near the 1000-m isobath at a site (C9; 72.46°N, 156.55°W) north of Utqiaġvik (previously Barrow), Alaska. The goal of these deployments was to better understand the flow along the slope and the fate of

Chukchi Shelf water exiting Barrow Canyon. Data and handling methods are described in section 2. Results are presented in section 3, including: vertical structure and temporal variability of currents and temperature at C9, relationship of sea ice and winds to flow patterns, variability of Atlantic water and the strength of the AOBC. Section 4 provides a discussion and summary of the results and conclusions.

2. Data sources and methods

2.1. Atmospheric variables

Two different reanalysis products were considered in order to provide a comprehensive record of wind over our region of interest. The first is the European Centre for Medium-Range Weather Forecasts (ECMWF) ERA5 reanalysis (https://climate.copernicus.eu/climate-reanalysis), which is the latest update to the ERA-Interim reanalysis (Dee et al., 2011). Like ERA-Interim, ERA5 solutions are based on a 4D-Var data assimilation routine, but the ERA5 model implements substantial improvements relative to ERA-Interim and include hourly output at 31 km horizontal resolution (Haiden et al. 2017; Hersbach et al., 2018). At present, no thorough validation exists for ERA5 in the Alaskan Arctic, but we note that an Arctic-focused comparison of seven reanalysis products found that ERA-Interim was among the top-performing models for a number of key parameters (Lindsay

et al., 2014). For 10-m winds, which is our focus, ERA-Interim had low biases of ≤0.5 m s^{-1} as well as the highest correlations (≥0.85) among the seven different reanalysis models when compared to independent daily-averaged wind records measured from drifting ice stations (Lindsay et al., 2014). Belmonte Rivas and Stoffelen (2019) discuss improvements of ERA5 wind relative to ERA-Interim in comparisons with Advanced Scatterometer satellite wind on a global scale, including a 20% improvement in root mean square wind speed agreement, and reductions in divergence and curl biases; the Arctic, however, was not part of that analysis. Given the model and resolution improvements of ERA5 relative to ERA-Interim, we anticipate model skill that is at least on par with that of ERA-Interim in the Arctic.

The second reanalysis product that we considered is the National Center for Environmental Prediction (NCEP) North American Regional Reanalysis (NARR). It is an extension of the NCEP Global Reanalysis that is run over the North American Region with improvements in both resolution (~32 km) and accuracy (Mesinger et al., 2006). Stegall and Zhang (2012) reported moderate agreement between coastal land- and ocean-based wind observations in northern Alaska and the NARR winds, with correlations of 0.66 for speed and 0.71 for direction. NARR wind variance was close to observed wind variance, but NARR wind speeds were biased low (by as much as 2.5 m s^{-1}). Moore et al. (2008) and Renfrew et al. (2009) reported somewhat better performance in comparisons to buoy and aircraft measurements off southern Greenland (correlations of 0.88 for speed and ≥0.92 for direction with a ~1.5 m s^{-1} low bias). NARR data are available eight times daily from

1979 to present. Three-hourly winds at 10 m were obtained from the NOAA Earth System Research Laboratory, Physical Sciences Division in Boulder, Colorado, USA, from their website (https://www.esrl.noaa.gov/psd/).

For both reanalysis products, data spanning 2014–2017 were downloaded and then linearly interpolated onto desired locations or averaged over specific regions discussed in the text. Because grid-scale noise is present in NARR wind, we first applied a two-dimensional Gaussian filter (standard deviation = 1; 5 grid points wide) to the spatial wind fields before calculating wind stress curl. We then re-gridded the smoothed NARR wind fields onto a regularly spaced 0.2° latitude by 0.6° longitude grid. Wind stress for both NARR and ERA5 was then estimated at each grid point following Large and Pond (1981), and wind stress curl was calculated using a centered-difference approach.

Comparisons with observed wind from the Barrow Atmospheric Baseline Observatory near Utqiaġvik, Alaska, were also made. Hourly averaged meteorological data recorded at the Barrow Observatory were downloaded from the NOAA ESRL Global Monitoring Division website at https://www.esrl.noaa.gov/gmd/obop/brw/.

2.2. Sea ice

Sea-ice concentration data (2014–2017) used herein were the daily Version 3 Sea-Ice Concentrations from Nimbus-7 SMMR and DMSP SSM/I-SSMIS and were obtained from the National Snow and Ice Data Center (http://nsidc.org/data/nsidc-0079). These data are calculated using NASA's Earth Observing System AMSR-E bootstrap algorithm. Average ice

concentrations in a 50 km × 50 km square around the mooring site (72.5°N, 156.5°W) were calculated.

2.3. Moorings

Moorings at C9 were deployed in three consecutive years (spanning September 2014 – July 2017) in ~1000 m of water on the Chukchi continental slope northwest of Barrow Canyon (Fig. 1, Table 1). For reference, this site was ~9.8 km offshore of the seaward-most mooring (deployed during the previous year) discussed in Li et al. (2019). Because of the steepness of the slope and the interference of sea ice during deployment, actual C9 bottom depths ranged from 870 m to 970 m. The mooring design included three RCM current meters near ~900 m, ~600 m and ~300 m; an upward looking 75 kHz acoustic Doppler current profiler (ADCP) at a depth of ~300 m; and a Sea-Bird Electronics (SBE) Microcat near a depth of 400 m (actual instrument depths are listed in Table 1). Additional temperature sensors (miniature temperature recorders or MTRs, and SBE-37 which also measures conductivity) were added in the upper 300 m for the 2016 deployment. Data were collected at hourly intervals except for the ADCP deployed in 2014, which recorded data at 2 h intervals. All instruments were calibrated prior to deployment and data were processed according to manufacturers' specifications. Current meter time series were low-pass filtered with a 35 h, cosine-squared, tapered Lanczos filter to remove tidal and higher-frequency variability, and then resampled at 6 h intervals. Additional analyses were completed using other filters as described in the text (e.g., section 3.4.1). Final processed time series data are accurate to at least ±0.002 °C, ±0.0005 S/m and ±0.5 cm s^{-1} (temperature, conductivity and currents, respectively).

Wavelet analysis was used to examine the dominant frequencies of the low-pass filtered current data. The wavelet function used here was the Morlet wavelet with non-dimensional frequency six, consisting of a sinusoid modulated by a Gaussian. The wavelet power spectra were normalized by the variance of each time series. The 95% significance levels were calculated by comparing each wavelet power spectrum to a red noise background spectrum, modeled as univariate lag-1 autoregressive (AR-1) processes generated with variance equal to that of each time series (Torrence and Compo, 1998).

2.4. Satellite-tracked drifters

From 2012 to 2018, the National Oceanographic and Atmospheric Administration's Ecosystem Fisheries Oceanographic Coordinated Investigations (EcoFOCI) program deployed 45 satellite-tracked drifters in the Chukchi Sea. Drifters were drogued at a depth of 25–35 m using a 10-m long "holey sock" drogue. Each drifter reported position and sea surface temperature via Argos approximately 14 times per day. Data were examined and spurious points were removed by inspection, as were data collected after drogues were lost (as indicated by a sensor), and after drifters grounded or entered into ice (determined from satellite maps of sea-ice extent). The resulting data were linearly interpolated to hourly intervals.

Lagrangian velocities were determined by centered differences using the hourly drifter positions. A low-pass filter (25-h running mean) was applied to the drifter location data. Spatially gridded mean velocities were then calculated following Stabeno and Reed (1994) and Stabeno et al. (2016b). In this analysis, each 2-day period within a grid area was considered an

independent estimate. Each rectangular grid cell was 1° latitude by 3° longitude. In addition, three rhomboids of a similar size abutted the slope (Fig. 2).

2.5. Shipboard hydrography

In this paper, temperature and salinity data from a cruise aboard the R/V *Ocean Starr* in late summer 2017 are presented. Conductivity, temperature, depth (CTD) profiles were collected using a Sea-Bird Electronics (SBE) 911*plus* system with dual temperature, conductivity (for salinity) and oxygen (SBE-43) sensors, and single chlorophyll fluorescence (WET Labs WETStar WS3S) and photosynthetically active radiation (PAR; Biospherical Instruments QSP-200 L4S or QSP-2300) sensors. Data were recorded during the downcast, with a descent rate of 15 m min^{-1} to a depth of ~30 m, and 30 m min^{-1} at deeper depths. Salinity calibration samples were taken on approximately one-third of the 135 casts and analyzed on a laboratory salinometer. The bottle samples were then used to post-calibrate the CTD data.

In addition to the 2017 R/V *Ocean Starr* data, historical CTD profiles collected aboard a variety of other vessels that were seaward of the shelf-break, within 200 km of the C9 mooring location, and at least 400 m deep are used to describe mean water properties over the Chukchi continental slope. Those historical profiles were taken from the much larger accumulated data set provided by Corlett and Pickart (2017).

3. Results and Discussion

3.1 *Patterns of variability of flow in the Chukchi Slope Current*

3.1.1. Spatial patterns of flow

Trajectories from satellite-tracked drifters (yellow lines Fig. 2a) provide information on general flow patterns during the ice-free season. Drifters deployed in the southern Chukchi Sea (south of 70°N), generally followed one of two trajectories, one northward through Central Channel and the other westward then turning northward through Herald Canyon. Most of the drifters did not enter onto Hanna nor Herald shoals (Fig. 2a). Stabeno et al. (2018) calculated that ~40% of the transport through Bering Strait exits through Barrow Canyon as part of the Alaskan Coastal Current (ACC). The ACC has a buoyant low salinity core, but similar to the Alaska Coastal Current in the Gulf of Alaska (Stabeno et al., 2004, 2016a), it is wind driven and extends beyond the freshwater core, with the strongest transport in the summer when northward winds dominate the Chukchi Sea. Only about half of the drifters deployed in the Chukchi Sea exited the shelf. The remainder failed to reach the northern boundary before sea ice arrived or before the shifting winds weakened the northward flow. Strong wind-driven reversals are evident in the 2017 (magenta) trajectory (Fig. 2a). It must be noted that except for the low-salinity Alaskan Coastal Water, the water in the ACC is more saline and denser than the melt water that typically resides along the slope. When exiting Barrow Canyon, the ACC water sinks to ~40 m (Stabeno et al., 2018). Thus, once seaward of Barrow Canyon the drifters are not tracking shelf water.

Most of the drifters deployed over the eastern Chukchi continental shelf traveled northward through Central Channel and turned eastward south of Hanna Shoal (Fig. 2; Stabeno et al., 2018). This flow intensifies between Icy Cape and Wainwright into a narrow current (the ACC) that exits the shelf via Barrow Canyon (Stabeno et al., 2018). The trajectories of flow,

once the drifters have exited Barrow Canyon, fall into three patterns (Fig. 2a): (1) a sharp westward turn and then continuing along the slope (blue); (2) an eastward turn for a short period (days) followed by a westward trajectory along the slope (magenta); and (3) eastward flow on the Beaufort shelf or along the shelf break (red). Of the 22 drifters that passed through Barrow Canyon, nine followed the first pathway and an equal number followed the second pathway traveling eastward for ~8 days (on average) before turning westward; only four followed the third pathway. The remainder of the 45 drifters that were deployed in the Chukchi Sea did not leave the shelf.

Of the satellite-tracked drifters that joined the westward flowing CSC, most continued northwestward along the slope until sea ice arrived. The remaining drifters ceased transmitting or lost their drogue before the arrival of sea ice. Mean Lagrangian velocities of all of the satellite-tracked drifters that transited along the continental slope were calculated as described in section 2.4, with an integral time scale of 48 h. Velocity was calculated in seven boxes (three rhomboids and four rectangles; Fig. 2). The outflow from Barrow Canyon dominates in the easternmost box. The velocity estimated in this box is biased, because all drifters were deployed on the shelf, so northward flow out of Barrow Canyon dominates the mean flow. The next three boxes (moving westward) all show a well-defined CSC (black arrows, Fig. 2b). Mean velocities from east to west were 14.9 ± 2.7 (mean ± standard error), 19.4 ± 2.5, and 17.3 ± 2.9 cm s^{-1}, respectively. Fewer drifters survived long enough to travel west of 165°W, and the velocities decreased from 14 ± 3.0 to 9.2 ± 1.6 cm s^{-1} in that region. The mean velocity (at 50 m) from the moorings (red arrow) was weaker than that calculated from the drifters for three reasons. Drogue depths were typically shallower than the uppermost ADCP bin; the Lagrangian velocities were

primarily during the summer and early fall months (July – November) when the CSC is at its strongest; and the drifters only entered the CSC when the currents were westward.

The trajectories of drifters in the CSC were often characterized by meanders (wavelength ~100 km). Eddies also were apparent in two trajectories (one is illustrated in Fig 2a) with radii of 25–50 km. The drifters remained near the slope in a ~70 km wide band, which is similar to the width of the CSC observed by Corlett and Pickart (2017).

It must be noted that the drifter trajectories reveal flow that is limited to the ice-free period. Once entering the ice field the drifters move with the sea ice. A few drifters transmitted locations sporadically during the winter, but most drifters caught in the sea ice were damaged and failed during winter or in spring/summer with the melting of the sea ice.

3.1.2. Temporal variability and vertical structure of flow at C9

Year-long deployments of each C9 mooring were made in late summer of 2014, 2015, and 2016, resulting in 34-month long velocity, temperature and salinity records at a variety of depths (Table 1; Figs. 3–5). During the first two deployments, sea ice arrived in the vicinity of C9 (50 km × 50 km box centered on the mooring site) in October and reached >80% areal ice cover within a month (Figs. 3 and 4, top panels). In the fall of 2016, sea ice arrived a month later in November, with >80% areal cover occurring ~3 weeks later (Fig. 5). Each year, the ice retreat began in June, with areal ice coverage falling below 20% from mid-July to early August.

The current meter records reveal a well-organized flow (Figs. 3–5). In the upper 100 m, the net direction ranged from 300 to 324° (Table 2), which is approximately the along-slope direction at C9. The principal axes were in a similar direction, indicating that most of the variance was also in the along-slope direction. Contours of monthly mean along-slope currents

(toward 310°) reveal the mean structure of the surface-intensified CSC (Fig. 6a). During the warm months, the CSC extended to depths of approximately 200–250 m depending on the year, which is consistent with the mean geostrophic description constructed from historical hydrographic profiles by Corlett and Pickart (2017), the modeling results of Watanabe et al. (2017) and the results presented in Li et al. (2019). There was a strong seasonality in the flow, with northwestward flow most common in the warm season, and reversals occurring below 200 m in the cold seasons of 2015 and 2016. September through November of 2016 showed southeastward flow from the surface to at least 500 m (Figs. 5, 6).

The current measurements deeper in the water column (>250 m) reveal the existence of an along-slope undercurrent that flows southeastward for at least part of the year (Figs. 3–5, Table 2). At C9, daily magnitudes of this southeastward flowing undercurrent were ≤10 cm s^{-1}. At ~300 m, there was a strong seasonality in the flow, with northwestward flow during spring shifting to southeastward flow in September 2015, June 2016 and July 2017 (Fig. 6b, solid line).

While the areal sea-ice concentration, and the flow in the upper 200 m and at 300 m all have annual signals, it is not clear that they are related. Depth-averaged flow in the upper 200 m ($V_{0\text{-}200}$) begins to increase before ice retreats in the summer and begins to weaken before the arrival of sea ice in the fall. The relationship between flow in the upper 200 m and at 300 m also appears to be somewhat out of phase, with northwestward flow at 300 m (Fig. 6b, solid line) tending to reverse just as the depth-averaged flow in the upper 200 m reaches its maximum.

On shorter time scales (days to weeks), variability, including flow reversals, was common in both the CSC and the flow below ~200 m (the AOBC; Figs. 3–5). The near-bottom (~900 m) flow was extremely weak during the first two deployments and not statistically

different from 0 cm s^{-1}. In the third deployment, the bottom instrument was almost 100 m shallower than during the first two years. During this last year, near-bottom currents were stronger and appeared to be related to the flow above (Fig. 5).

3.1.3. Vertical variability

To examine the vertical structure of the currents in more detail, we divide the time series into two parts—the warm (ice free) season (1 July – 31 October) and the cold (ice-covered) season (1 December – 31 May). During the warm season, currents in the upper 200 m were much stronger in 2015 than they were in either of the other years (Fig. 7a). During the cold season, the three years were all comparable (Fig. 7b). A comparison of average flows during the warm and cold seasons shows that currents in the upper 200 m were stronger in the warm season compared to the cold season, as were the reversals below 300 m (Fig. 7c). Reversals were evident below 300 m in the warm season. During the cold season, average currents below 300 m were weak and were not significantly different from zero.

The currents fall into three vertical groups: (1) 0–200 m; (2) 200–850 m; and (3) below 850 m (Fig. 8). Currents in the upper 200 m were well correlated and in phase during each deployment, and the rotation between different depths was near zero. The second vertical group was also in phase and well correlated, with a slightly larger angle of rotation among depths. Currents in groups 1 and 2 were significantly correlated at zero lag, but with a rotation angle of 15–30°. The final group consists of the bottom instrument in the first two deployments. Here the correlations between group 3 and the other two groups were weak, with significant correlation largely limited to group 2. Perhaps more importantly, there was significant rotation of ~140° counter-clockwise and a lag of 2 days between the currents at ~900 m and those at depths > 200

m. The third deployment was approximately 70–100 m shallower than the other two deployments and the bottom two depths were significantly, albeit weakly, correlated and in phase with group 2.

This same vertical pattern appears in the empirical orthogonal functions (EOFs) of the along slope component (along 310°) of the time series for each deployment (Fig. 9). There were two significant modes, EOF1 and EOF2. EOF1 accounted for 69%, 51% and 62% of the variability in the 2014, 2015 and 2016 deployments, respectively, and EOF2 accounted for 17%, 33% and 22% of the variability in the 2014, 2015 and 2016 deployments, respectively. EOF1 represents the upper ~250 m of the water column, and EOF2 represents the flow patterns between ~250 and ~850 m. The bottom time series of the 2014 and 2015 deployments were not represented in neither EOF1 nor EOF2 and appeared as a mode by itself that was not statistically significant.

3.2 *Temperature and salinity at the mooring site*

Several water types are recognized on the Chukchi Shelf (Coachman et al., 1975; Gong and Pickart, 2016; Corlett and Pickart, 2017) and are indicated in Fig. 10a. Melt water (MW) results from melting ice earlier in summer. The source of fresh, relatively warm Alaskan Coastal Water (ACW), and the colder more saline Bering Sea Water (BSW) originates in the Bering Sea, entering the Chukchi Sea through Bering Strait. The cold, saline Winter Water (WW) forms locally through cooling and brine rejection during the previous winter. Remnant Winter Water (RWW) forms as WW warms through heating and mixing processes in the Chukchi Sea. Finally, the relatively warm and saline Atlantic Water (AW) originates in the Atlantic, as its name suggests, flowing cyclonically around the Arctic basin and, occasionally, flows onto the Chukchi Shelf via

Barrow Canyon (Bourke and Paquette, 1976; Ladd et al., 2016; Wood et al., 2018; Pisareva et al., 2019).

The C9 data at 45 m in 2016 showed large variability in temperature and salinity, indicating multiple water types (MW, RWW, BSW; cyan dots, Fig. 10a). Salinity varies from <30 to >32, with the least saline water occurring in early December, almost a month after the arrival of sea ice (Fig. 11a), and likely is the result of local ice melt. So, it was not surprising that the water type for this least saline, cold (<-1°C) water is categorized as MW (Fig. 10a).

While measurements of salinity were limited to a few depths, in the 2016–2017 deployment 11 temperature sensors were distributed between 45 m and 460 m (Fig. 11b). In the upper 100 m, temperature ranges from -1.8°C in winter to 3.5°C in July 2017 after ice retreat (Fig. 10a). Between 100 m and 200 m, there was a band of relatively cold (approximately -1°C) water. At ~200 m, the temperature begins to increase from approximately -1°C reaching 0°C at 258 m ± 10 m (average ± standard deviation) and continuing to warm to a depth of ~400 m. This relatively warm, saline (~0.5°C, 34.8; Fig. 10b) water below 200 m is Atlantic Water (AW).

Atlantic Water generally inhabits intermediate depths (200–1000 m) over the continental slope in the western Arctic (Corlett and Pickart, 2017). AW contains a large amount of heat (enough to melt all the ice in the Arctic, if it came into direct contact with sea ice; Polyakov et al., 2017). At the C9 location the core of this water mass, with maximum subsurface temperature ~0.65 °C (0.57–0.80 °C) and practical salinities in the range of 34.73–34.86, was consistently found near a depth of 400 m (Fig. 10b) as expected from the historical data (Fig. 10 c–d). The C9 instrument depths varied from 345 m to 460 m dependent upon the year. The 2016 deployment was the deepest (~460 m), and the 2014 deployment was shallowest (~345 m), with the 2015 deployment falling in between (~382 m). All three time series were near the relative maximum in

temperature of AW, and varied as expected along the long-term temperature-salinity line. The greatest variability was in the 2014 deployment, which was at the upper edge of the depth of the local temperature maximum. The least variability was at 460 m, while the two shallower instruments showed periods of decreasing temperatures.

3.3. *Temporal variability in the depth of Atlantic Water*

To examine the temporal variability in the depth of the warmer Atlantic Water, we chose the 0°C isotherm (Fig. 11b). There was insufficient vertical instrumentation near 350 m, where the relative maximum of temperature occurs and the water column at the relative minimum (depth <200 m) is influenced by surface processes. The character of the isotherm varies in time. From September through March, there was much higher variability in the depth of the 0° isotherm than later during April – July. This coincides with the variability of the currents (Fig. 5, bottom). At depths shallower than 170 m, prior to mid-March, the currents were highly variable and largely southeastward. This transition was not related to sea-ice cover, since sea-ice cover was extensive (>90%) from mid-January through April (Fig. 5, top).

There are two sharp increases in the depth of the 0°C isotherm, one in late October and the second in late December (Fig. 11b). The first event was during a period of no ice and the second during extensive ice cover. Both events had temporal scales consistent with those of longitudinal waves (3–5-day periods; Fig. 12). Interestingly, the greatest depth of the 0° isotherm in October (on the 24th) occurred when the currents were northwestward and the greatest depth of the 0° isotherm in December (on the 27th) occurred when currents were southeastward, but both were during a period of maximum wave amplitude (~20 cm s^{-1}).

Energy in the 3–5 day band is fairly common in the along slope currents at ~240 m (Fig. 13b). It does not appear to be strongly related to the presence of sea ice nor to variations in the winds. At periods >12 days there are only a couple of events in the fall of 2015 and 2016 with significant energy. In contrast, the spectra of the depth-averaged along-slope currents in the upper 200 m appears to be more energetic when sea-ice concentrations are <85% areal coverage (Fig. 13a). There are several periods (e.g. late March 2015) when a sharp decrease in sea ice is associated with an increase in energy at 1–5 days. There also is more energy in the 10- to 20-day band, but once again no significant peaks in energy are present at lower frequencies.

3.4. *Forcing mechanisms*

3.4.1. Wind

Given the lack of buoy measurements of wind in the Chukchi-Beaufort region, the ECMWF ERA5 reanalysis product was chosen for our analysis. While we also evaluated the NCEP NARR reanalysis, comparisons with observed wind from the Barrow Atmospheric Baseline Observatory near Utqiaġvik, Alaska, indicated that ERA5 more faithfully reproduced the observations. Zero-lag correlation coefficients for the east-west (north-south) components of 10-m winds spanning the 2014–2017 C9 record were r = 0.96 (0.85) for ERA5 compared to 0.90 (0.70) for NARR. Complex (vector) correlations were r = 0.94 with a 4° clockwise rotation for ERA5 wind compared to observed wind, while NARR wind had r = 0.89 with a 17° clockwise rotation relative to the Barrow observations. As is discussed later, the use of a reanalysis product such as ERA5 further allows for an examination of the spatial structure of the wind field.

We attempted a number of different lagged correlation analyses between both observed and ERA5 winds and the along-slope currents measured at the C9 mooring. For simplicity, we first chose to use currents from the shallowest ADCP bin (52 m, 36 m and 44 m depth for the 2014, 2015 and 2016 deployments, respectively). Correlations between year-long records of low-pass filtered 10-m ERA5 wind interpolated to the C9 location and the low-pass filtered near-surface along-slope current were poor, even when the current was lagged relative to the wind. The highest correlation coefficient ($r = 0.36$ at zero lag for the cross-slope wind component) was in 2015. This was the year with the shallowest (36 m) current data. Using observed wind or wind stress from the Barrow observatory did not markedly improve the wind-current correlations. Similarly, when we restricted the analysis to the largely ice-free summer season (or conversely to the ice-covered winter season), wind-current correlations remained poor or not significant, despite the ice-free periods generally resulting in stronger relationships. The highest correlation coefficient during an ice-free period was $r = 0.46$ for the along-slope wind in fall 2014. Correlations between near-surface currents at C9 and remote ERA5 winds at selected sites (e.g. in the East Siberian Sea as suggested by Danielson et al., 2014; Peralta-Ferriz and Woodgate, 2017) were generally lower than with local winds, even with lags.

We next examined wind-current correlations using successively low-frequency filters (5, 10, 15 and 30 day Hanning windows) for both the observed wind and along-slope current records. Again, highest correlations were in 2015, but the values remained low (e.g. $r = 0.42$ for the cross-slope component of wind with a 15-day Hanning filter applied). Unsurprisingly, correlations between ERA5 wind and the 200-m depth-averaged along-slope current, $V_{0\text{-}200}$, over the entire 3-year record (also using 5, 10, 15 and 30-day Hanning window filters) were also poor.

Thus, near-surface along-slope flows at C9 do not appear to be significantly correlated with local wind nor with ERA5 wind at select remote sites.

However, there are specific events in the C9 200-m depth average current record, $V_{0\text{-}200}$, that appear to be in response to local wind forcing (Fig. 14c). For example, the onset of a period of sustained southeastward along-slope flow in September 2016 begins during a reasonably strong southeastward wind event (Fig. 14). Interestingly, such strong along-slope wind events are somewhat rare in the 3-year record, with the September 2016 event being the strongest during an ice-free period. Similarly, the enhancement of northwestward slope flows in April 2017 may be related to the northwestward component of winds at that time. Recall that it is evident from the wavelet analysis (Fig. 13a) that more energy is found in the currents (2–10 day band; 0–200 m average) when areal ice concentrations are <85% and wind can directly force the ocean surface. April through June 2017 was a period of relatively sustained upwelling favorable winds (Fig. 5, top) with corresponding low variability in the depth of 0° isotherm (as mentioned in the previous section; Fig. 11b) and a period of reduced 3–5 day energy in the currents (Fig. 13a). During this time, correlation between the winds and depth of 0° isotherm were significant ($r = 0.48$, $p < 0.01$) with the isotherm depth lagging the winds by 1 day with a decrease in depth of 1.8 m per 1 m s^{-1} increase in wind toward 310° (approximately northwestward). The winds were not well correlated ($r = 0.22$, $p>0.10$) with the depth of the 0° isotherm for the first part of the record (September 2016 – February 2017). We note that Li et al. (2019) also found no correlation between local wind forcing and upwelling events on the Chukchi continental slope at their nearby array site. Watanabe et al. (2017) similarly noted the lack of correspondence between local winds and the current flowing west along the Chukchi Slope in their model.

To briefly summarize, although more synoptic energy (2–10 day band) is found in the upper water column currents during ice-free periods, on average, local wind does not appear to exert a primary influence on the upper water column along-slope current at the C9 site. Evidence suggests that particularly strong wind events may enhance upper water column currents over the slope, consistent with the findings of Corlett and Pickart (2017). For at least a portion of the C9 data record in 2017, wind influences were instead more readily observed in variation of the depth of the 0° isotherm.

3.4.2 Wind stress curl

Because the C9 mooring was located >100 km from shore, it is unlikely that coastal divergence of surface Ekman transport would be an important mechanism there. Wind stress curl, however, could lead to transport divergence or convergence that, in turn, could drive flow along the continental slope. Using composite averages over multiple northwestward flow events, Li et al. (2019) showed relationships between strong along-slope flows and the wind stress curl averaged over a region of the northeast Chukchi Shelf, suggesting that wind stress curl is a primary forcing agent for strong and weak states of the CSC. Although such extreme states comprised only ~23% of their record, their dominant EOF mode appeared to reflect that variability, suggesting it may be important.

To investigate whether or not wind stress curl impacts currents at C9, we plotted the time variation of mean wind stress curl calculated over a similar portion of the northeast Chukchi Sea shelf (as in Li et al., 2019; Fig. 14a) and compared it with the upper 200-m depth-averaged along-slope current, $V_{0\text{-}200}$, (Figs. 14 d,g). A few characteristics stand out. First, wind stress curl averaged over the northeast Chukchi Shelf is highly variable, often changing sign in as little as

three days. On average, the mean wind stress curl is negative, although a few positive events are apparent such as in August 2015, February 2016, and January 2017. Negative wind stress curl over the northeast Chukchi Shelf would lead to flow convergence and geostrophic sea level set-up. Interestingly, high sea level over the shelf (relative to sea level offshore) would tend to force southeastward along-shelf/slope flow, which is opposite to the mean northwestward flow observed at the C9 location (Fig. 14g) and as previously observed for the CSC (Corlett and Pickart, 2017; Stabeno et al., 2018; Li et al. 2019). Thus, on average, it does not appear that the mean wind stress curl over the northeast Chukchi Shelf is itself adequate to explain the observed northwestward flowing CSC at the C9 site. Still, as with some of the wind events described earlier, and in agreement with Li et al. (2019), there is a suggestion of correspondence between portions of the wind stress curl record and the mean along slope currents. For instance, the current decreases and briefly turns southeastward in October and December 2015 when the wind stress curl is strongly negative. Similarly, the current increases to the northwest in early January 2017 when the wind stress curl is significantly positive. Other events exist, however, that defy such a simple one-to-one explanation. The strengthening of the current in July 2015, a time when the wind stress curl over the northeast Chukchi Shelf was in opposition, is not clearly explained by shelf-average curl. Also, the positive current events spanning June–August 2016 do not appear to be related to wind stress curl over the shelf.

An examination of monthly averaged spatial patterns of wind and wind stress curl throughout the region suggests the possibility of large gradients in wind stress curl near the Chukchi continental slope (not shown); in some cases, positive/negative wind stress curl over the shelf was accompanied by negative/positive wind stress curl offshore. Thus, the induced across-slope geostrophic sea level gradient could potentially be enhanced or diminished as a result of

changes in the sign of the wind stress curl across the continental slope. To test this possibility, we averaged wind stress curl over two adjacent boxes: one including a small region of the Chukchi Shelf west of Barrow Canyon parallel to the continental slope, and the other immediately offshelf including the continental slope (Fig. 14a). The difference in mean wind stress curl over these two boxes (shelf value – offshelf value) is illustrated in Fig. 14e. The mean wind stress curl difference is negative, meaning that the wind stress curl induced geostrophic sea level in the offshore box is higher than that over the shelf box (ignoring any otherwise pre-existing shelf-slope sea level gradient), a condition that would favor the northwestward flowing CSC. There is also the suggestion of correspondence between events in the wind stress curl difference and the mean along slope currents. For example, the along-slope current is strong from August through September 2015 when the curl difference is favorable, and then decreases as the curl difference changes sign in late September 2015. A similar series of events occurred during fall 2016. Nevertheless, correlation between the shelf-offshelf curl difference and the 200-m depth-averaged current remains poor over the entire record, even when considering low-pass filtered time series (Figs. 14e, g).

3.4.3. The Beaufort Gyre

The Beaufort Gyre (BG) is a relatively shallow (~250 m), anticyclonic circulation that dominates the Canadian Basin and is driven by the Beaufort Sea High pressure system (e.g. Giles et al., 2012; Moore 2012). The low salinity (<30) core of the BG sits above more saline Atlantic Water. It is of interest that the depth of the BG along its edge shoals to ~200 m (Doddridge et al., 2019; see their Fig. 1), which is the depth between our observed current groups 1 and 2 discussed in section 3.1.3. The size and strength of the gyre varies on seasonal through interannual time

scales. Using sea surface height data from satellite altimetry during the period 2003–2014, the area of gyre and its strength were greatest in the fall and smallest in the summer (Regan et al., 2019). In addition, the size and strength of the BG increased during this time period. Although care must be taken in interpreting dynamic ocean topography near shore and complex bathymetry, it is noteworthy that the edge of the gyre extends in recent years along the continental slope from 130°W westward to the Chukchi Borderland (Fig. 2b).

The location of C9 is at the southern edge of the BG, so it could be argued that the currents measured at C9 are likely related to the BG. The largest slope of dynamic ocean topography is in the region of C9 westward to the Chukchi Borderland (Regan et al., 2019; see their Figs. 4–5), where the outer edge of the gyre crosses lines of latitude. This is reminiscent of a western boundary current. Here the bathymetry of the shelf crosses lines of latitude effectively reducing the strength of β, the rate of change of the Coriolis parameter (f) with latitude, to ~20% of its value at a latitude of 45°. Yang et al. (2016) suggest that even though β is small at these latitudes a western boundary current could be supported.

Since the BG is driven by the large-scale wind stress curl it is possible that variability in upper 200-m depth-averaged current at C9 would also be related to variability in the basin-scale wind stress curl. A time series of wind stress curl averaged over the Canada Basin is illustrated in Fig. 14f. As with other wind metrics, correlation of this low-pass filtered quantity with low-pass filtered currents was poor ($r = 0.12$ at 37-day lag with a 30-day Hanning filter applied). We also attempted to correlate the currents with running cumulative sums of basin-averaged curl (e.g. summations over 60 days and 90 days), but this too gave similarly poor results.

3.4.4. The Alaskan Coastal Current exiting Barrow Canyon

Using both an idealized model and the year-long moored array observations of Li et al. (2019), Spall et al. (2018) found a relationship between flow in Barrow Canyon and the CSC, with monthly-averaged CSC transport lagging the transport through Barrow Canyon by roughly 2–3 months. Using the Barrow Canyon transport and velocities measured at C9, our results are more ambiguous.

The mean northeastward flow out of Barrow Canyon is ~0.5 Sv (Itoh et al., 2013; Stabeno et al., 2018), with a seasonal signal. The monthly mean transports in Stabeno et al. (2018) were calculated from hourly currents measured at three mooring sites located off Icy Cape. The number of instruments available varied from three ADCPs deployed in September 2010, 2016, 2017 and 2018 to only one instrument at the central site in 2012. Details of the calculations can be found in Stabeno et al. (2018). The monthly mean northeastward transport along the Chukchi Shelf is strongest in the summer months and weakest in the winter months. As the flow exits Barrow Canyon much of it continues northwestward in the CSC, while a smaller portion turns east forming the Beaufort shelf break current (Nikolopoulous et al., 2009). There is a significant correlation between the monthly mean transport in Barrow Canyon and the upper 200-m depth-averaged velocity, $V_{0\text{-}200}$, observed at C9 ($r = 0.5$, $p<0.01$; Fig. 15). This significant correlation, however, is a result of six individual months during which the flow in the CSC is above average (Fig. 15a). That is, when monthly mean flow in the CSC is strong, the transport exiting the shelf through Barrow Canyon is also strong. There are even more instances, however, when the Barrow Canyon transport is just as strong yet the monthly averaged flow in the CSC is weak (<10 cm s^{-1}).

As alluded to above, we do not observe a 2–3 month lag between the peaks of monthly-averaged Barrow Canyon transport and currents at C9, although the variability in our record is

substantial (Fig. 15). Given an approximate distance of 100 km from Barrow Canyon to the C9 mooring, currents leaving Barrow Canyon should pass the C9 location in 6–17 days, assuming typical speeds of ~6 cm s^{-1} from C9 (Fig. 14g) and ~15 cm s^{-1} from the drifters (drogue depth ~30 m; Fig. 2b).

Thus, using the C9 and Icy Cape current observations the flow out Barrow Canyon does not appear to drive the CSC. Once again there does appear to be an intermittent relationship between possible forcing mechanisms and the magnitude of flow at C9. While the ACC does not drive the CSC, it is a major contributor as discussed in the next section.

3.4.5. Volume transport in the CSC

The transport estimate for the CSC can be updated using results from Li et al. (2019) and our C9 results presented herein. Li et al. (2019) estimated transport in the CSC using three year-long moorings deployed in 2013 (spanning 163–356 m bottom depths) and covering an off-slope distance of ~30 km. Their estimate of transport over this area appears to be ~0.35 Sv (their "non-mirrored" value). As noted earlier, our C9 mooring was on the same line of moorings, and ~10 km beyond their outermost site. If we assume that the measurements at C9 are representative of the 20 km beyond the Li et al. (2019) moorings and note that the mean along-slope current in the upper 250 m at C9 was ~5 cm s^{-1}, transport in this region is estimated at 0.25 Sv (width × velocity × depth = 20,000 m × 0.05 m s^{-1} × 250 m). This is likely an under-estimation since the satellite-tracked drifter trajectories provided a width estimate of ~70 km for the CSC. If we do the same calculation assuming that the C9 average velocity is representative of 40 km instead, we obtain an estimate of 0.5 Sv. Although this is likely an overestimation, it

provides a range of transport (including the Li et al. [2019] estimate of 0.35 Sv) in the CSC of 0.55 to 0.85 Sv.

The mean transport at the Icy Cape moorings for September 2014 – August 2017 was 0.42 Sv (following Stabeno et al., 2018). Nikolopoulos et al. (2009) estimated that the eastward transport of Pacific water exiting Barrow Canyon was 0.13 Sv, meaning that 0.29 Sv of the water exiting Barrow Canyon would flow westward. Using these values, the volume of outflow from Barrow Canyon provides between ~34% ([0.42-0.13]/0.85) to ~53% ([0.42-0.13]/0.55) of the CSC volume transport, which as a percentage is less than what was estimated by Li et al. (2019). Alternately, if we use the values explicitly measured from the mooring array, Li et al. (2019) estimated 0.28 Sv of Pacific water in the CSC (their "non-mirrored" value), which is essentially identical to our 0.29 Sv that exits Barrow Canyon and turns westward.

4. Discussion and Conclusions

Three years of moored current meter and water property data confirm a well-defined, seasonally varying northwestward surface-intensified flow (the CSC) along the northern Chukchi continental slope. This flow was best defined in the upper 200–250 m of the water column. Below this surface layer was an undercurrent (the AOBC) that flowed predominantly southeastward. Temperature and salinity in this undercurrent (~200 m to ~850 m) classified it as Atlantic Water. Vertical correlations among current time series in the AOBC were strong, as were correlations among current time series in the CSC. Only temperature was measured at 900 m in the 2014 and the 2015 deployments. The average potential temperature at 900 m (below the

AOBC) was ~0.0 °C (standard deviation of 0.03°C), which is typical of Arctic deep water in the Canada Basin.

The C9 mooring site was unknowingly positioned on the southern boundary of the BG (Regan et al., 2019). The BG intensified from 2003 through 2012, reaching a maximum in 2013 and 2014 the end of the analysis period described by Regan et al. (2019). In recent years, the geostrophic transport in the vicinity of C9 has stabilized (Armitage et al., 2017; Zhang et al., 2016), although there remains strong monthly variability in the system, particularly in the fall (Regan et al., 2019). Northwestward velocity appears to be largest in the fall (Regan et al., 2019), but variability also appears to be strongest at that time. In contrast, the flow in the upper 200 m at C9 increased from June through September and then appeared to weaken in the fall. It is unclear whether this apparent disagreement is a result of temporal variability in the system or other mechanisms. For instance, C9 was a single mooring, making it difficult to differentiate between spatial oscillations, such as cross-slope meanders, and temporal variability in the current system. As noted in section 3.1.2, meanders in the system are apparent in the satellite-tracked drifter trajectories. The northwestward trajectory of the drifters followed the trajectory of the southern edge of the BG in 2013 and 2014 (Regan et al., 2019).

The appearance of the CSC has been most evident to the west of Utqiaġvik, AK (Corlett and Pickart, 2017; Stabeno et al., 2018; Li et al., 2019). According to the analysis by Regan et al. (2019) this is also the region of greatest slope of dynamic ocean topography. Evidence for a similar current flowing along the Beaufort continental slope is currently lacking. However, we note that the ~1400 m depth mooring of Nikolopoulos et al. (2009) did capture a weak (~2 cm s^{-1}) mean northwestward near-surface flow. Interestingly, the Beaufort mooring array analyzed by Nikolopoulos et al. (2009) was deployed in 2002–2004 before the recent expansion and increase

in strength of the BG (Armitage et al., 2017; Regan et al., 2019). It remains unknown whether a more recent mooring array would detect a similar relatively weak northwestward flowing current off the Beaufort continental slope. Also, note that the model fields of Watanabe et al. (2017) showed northwestward flow all along the Beaufort continental slope. That the strength of the CSC varied substantially over the three years of our deployment is not surprising, in that the strength and size of the BG also varies interannually (Armitage et al., 2017; Regan et al., 2019).

Recent updates to the freshwater content volume in the BG region indicate that 2015–2017 have the largest total freshwater content volumes on record, with particularly large spatial gradients near the Chukchi continental slope (Proshutinsky et al., 2019; see their Figs. 4–5). Thus, our three years of observations at C9 were during a period where the BG was particularly strong.

Li et al. (2019) built upon the results of Corlett and Pickart (2017) by suggesting that wind stress curl over the shelf, rather than westward winds alone, primarily drive variability in the CSC. Our findings indicate that while this may be true in an episodic sense, it is generally not the case over our three-year C9 record. The along-slope currents at C9 were not significantly correlated with local winds, except at depths < 40 m. There are several possibilities for this.

One potential explanation for the lack of strong correlations between winds and currents at C9 could be meandering of the current. As mentioned, from a single mooring location, it is difficult to distinguish between temporal variability in currents and inherent spatial changes such as cross-slope meandering of the current.

Secondly, the winds were typically weak, often <10 m s^{-1} (Fig. 14b–c). At present, we remain uncertain about how skillfully the ERA5 reanalysis reproduces the true wind stress curl. Belmonte Rivas and Stoffelen (2019) suggest improvements in ERA5 relative to its predecessor

model, but additional ground-truthing is needed, particularly in the Arctic where data for assimilation is sparse.

Remote forcing could provide another possible explanation for the lack of correlation between currents and winds or between the depth of the 0° isotherm and local wind during the first part of the 2016–17 record. Recall that there was significant energy in the currents in the 2–10 day energy band. This energy is likely generated elsewhere, and thus could obscure any correlation between currents and local winds. While we tested for relationships with remote winds at select sites without satisfactory results, a more complete investigation of remote versus local forcing on the Chukchi continental slope is left for future analyses.

Finally, the C9 location is approximately 120 km from the coast north of Utqiaġvik, AK, where the coastline abruptly changes direction by ~90°. Wind at C9 is usually oriented northeast-southwest, roughly parallel to the Chukchi Sea coast (Fig. 14b; Stabeno et al., 2018), so that it often blows across, rather than along, the continental slope. This general lack of alignment of the wind and continental slope could potentially help explain the lack of correlation between the wind and observed along-slope currents at C9. In contrast, wind blowing along Alaska's Beaufort coastline, where the shelf is much narrower, appears to be effective at forcing along-slope flows (Nikolopoulos et al., 2009). Any oceanic response, however, to changes in wind forcing on the Beaufort continental slope would propagate east in the direction of coastal-trapped waves, rather than toward the C9 site. Finally, the BG is forced by basin-wide winds (the Beaufort High) and modified by the accumulation of freshwater stored in the BG (Armitage et al., 2017; Regan et al., 2019; Petty et al., 2016), so it is not surprising that the CSC at C9 is not locally wind-forced. Although we also found poor correlations between basin-averaged wind stress curl and currents at C9, the fact that the region of highest sea-surface height gradient exists

along the Chukchi continental slope from Barrow Canyon to the Chukchi Borderland (Regan et al., 2019) suggests a relationship between the CSC and the BG.

We hypothesize that this northwestward flowing CSC is forced by the edge of the Beaufort Gyre. Corlett and Pickart (2017), while admitting that a dynamical connection could exist, argued that the CSC was not a manifestation of the Beaufort Gyre, citing the relatively strong currents observed on the Chukchi Slope, lack of a similar current off the Beaufort Slope and the presence of Chukchi Shelf water properties in the CSC as evidence. Spall et al. (2018) similarly suggest that the CSC is distinct from the Beaufort Gyre owing to its Bering Strait source and unique water properties. Nevertheless, the fact that the CSC flowed west in the model of Spall et al. (2018) was a result of the basin-scale circulation associated with the BG (their Fig. 16). The body of evidence indicates that the fact that the CSC flows northwestward is a result of the BG dynamics. We suggest that water exiting the Chukchi Shelf via Barrow Canyon is entrained into the western boundary current of the BG flowing northwest along the Chukchi Slope, consistent with the model results of Spall et al. (2018). Dynamically, we expect that the lateral pressure gradient associated with the BG in the region north of, and extending west from, Utqiaġvik (Figs. 4–5 of Regan et al., 2019) presents an effective "wall" that is more than sufficient to overcome the Coriolis force acting on the flow emanating from Barrow Canyon, resulting in the CSC flowing northwestward along the continental slope.

The shelf-slope system from Barrow Canyon to the Chukchi Borderland is a complex region. The exit of warm, saline water out of Barrow Canyon during summer is a source of subsurface heat to the Arctic Ocean basin (Aagaard and Carmack, 1989; Stabeno et al., 2018; Woodgate et al., 2012). In contrast, the Atlantic Water can enter the Chukchi Shelf via Barrow Canyon (Bourke and Paquette, 1976; Ladd et al., 2016; Wood et al., 2018). An array of moorings

across the Chukchi Slope would provide insight into the variability in the boundary of the BG, its strength and the pathways of the outflowing Pacific Water. Clearly, additional observations are required to understand the system.

Acknowledgments

Support was provided by the National Oceanic and Atmospheric Administration; the Bureau of Ocean Energy Management CHAOZ, CHAOZ-X and ArcWEST programs; the NPRB Arctic Program (A92-02a, A92-02b); and the Joint Institute for the Study of the Atmosphere and Ocean (JISAO) under NOAA Cooperative Agreement NA15OAR4320063. This is contribution No.
4990 for Pacific Marine Environmental Laboratory and Contribution No. 2019-1048 to University of Washington JISAO. We thank three anonymous reviewers for helping to improve the manuscript.

Tables:

Table 1. The duration of deployment, location and bottom depth are indicated in the first column. The instrumentation and depth of instruments are indicated in columns 2–4. MTR refers to miniature temperature recorders.

Deployment/ Recovery Info	Instrument	Measurement	Deployment Depth (m)	Comments
14C9	75 kHz ADCP	Currents	345	16-m bins
10/1/14 – 9/15/15	SBE-37	Temp, Sal	349	
72° 27.5' N	RCM-9	Currents, Temp	350	Inst. at 645 m failed
156° 33.9' W	RCM-11	Currents, Temp	895	
950 m				
15C9	75 kHz ADCP	Currents	372	8-m bins
9/15/15 – 9/8/16	SBE-37	Temp, Sal	382	
72°28.0' N	RCM-9	Currents, Temp	378, 672	
156°33.0' W	RCM-11	Currents, Temp	922	
970 m				
16C9	75 kHz ADCP	Currents	290	16-m bins
9/8/16 – 8/3/2017	MTR	Temp	90, 101, 120, 150, 180, 210, 240, 270	
72°27.8' N	SBE-37	Temp, Sal	45, 460	
156°32.9W	RCM-9	Currents, Temp	311	
870 m	RCM-11	Currents, Temp	467, 822	

Table 2. Velocity statistics at selected depths distributed through the water column. Maximum speed was calculated from the hourly velocities, while net speed and principal axis were calculated from the low-pass filtered data (35-hr Lanczos).

Mooring	Depth (m)	Maximum Speed (cm s^{-1})	Net speed (Direction) (cm s^{-1} [°])	Prin. Axis (% var) (° [%])
14C9	48	72.1	10.6 (300)	302 (62)
	96	59.1	9.5 (302)	298 (62)
	192	31.1	3.4 (306)	320 (66)
	304	11.5	1.0 (291)	318 (75)
	895	11.4	0.5 (159)	359 (75)
15C9	35	58.6	8.0 (320)	306 (56)
	99	57.8	5.2 (327)	312 (58)
	195	35.9	1.7 (335)	318 (69)
	299	21.6	1.2 (129)	323 (79)
	672	17.0	1.4 (148)	330 (73)
	922	9.1	0.7 (160)	358 (75)
16C9	41	54.5	6.1 (324)	322 (70)
	105	48.7	4.7 (322)	320 (68)
	201	23.1	0.8 (10)	321 (75)
	265	17.4	1.6 (124)	320 (80)
	467	13.2	1.9 (148)	322 (77)
	822	14.4	0.8 (156)	319 (82)

Figure Captions

Fig. 1. Schematic map of surface flow patterns over the Chukchi Sea continental shelf and slope (adapted from Stabeno et al. 2018). The location of the C9 mooring, near the 1000-m isobath, is indicated with the black square.

Fig. 2. (a) Drifter trajectories (drogue depth ~30 m). The yellow trajectories indicate drifters deployed in the region. Three pathways are shown in different colors: (1) eastward flow on the Beaufort Shelf (red); (2) first eastward flow and then northwestward flow (magenta); and (3) northwestward flow upon exiting Barrow Canyon (blue). Selected dates are indicated along each trajectory. (b) The position of the edge of the Beaufort Gyre during four different years (adapted from Regan et al., 2019, their Fig. 3). The mean Lagrangian velocity of the drifters in each box (black arrows), with the number of independent estimates that contributed to the mean (black numerals). The red arrow is the mean velocity at ~50 m from the three C9 mooring deployments.

Fig. 3. (top panel) Daily ERA5 wind vectors interpolated onto the C9 mooring location and percent areal ice cover (blue) in a ~50 km × 50 km box centered on C9. (bottom panel) Low-pass filtered current velocities (daily) measured at C9 spanning September 2014 – September 2015. The depths of each time series of currents are indicated. Both the wind and velocity axes were rotated 310° so that upward is approximately northwestward along the continental slope. Note the different velocity scales.

Fig. 4. Same as Fig. 3 except for September 2015 – September 2016.

Fig. 5. Same as Fig. 3 except for September 2016 – August 2017.

Fig. 6. (a) Contours of monthly mean currents (rotated 310°) measured by the three ADCPs deployed at C9. Positive is approximately northwestward. At the top is the areal sea-ice cover (>20%) in the vicinity of C9. The shaded region represents negative (nominally southeastward) flow. (b) Monthly mean currents at ~300 m (solid line) and depth-averaged velocity, $V_{0\text{-}200}$, in the upper 200 m (dotted line). Positive is northwestward.

Fig. 7. Mean alongshore flow in (a) the warm season, 1 July – 31 October, and (b) the cold season, 1 December – 31 May. Positive is approximately northwestward (310°). Colored dots represent averages for different deployment years (2014 is red, 2015 is green, 2016 is blue). Solid lines in (a) and (b) represent 3-year seasonal means and are least squares fits of a third-degree polynomial. (c) The 3-year seasonal means are shown separately to facilitate comparison.

Fig. 8. Complex correlations (below diagonal) and correlation angles (above diagonal) for currents for each of the three mooring deployments: (top) 2014 with 1350 data points; (middle) 2015 with 1372 data points; and (bottom) 2016 with 1200 data points. Instrument depths are in meters. The correlations are color coded from dark (high) to light (low) correlations. Shaded correlations are significant at $p<0.01$. All lags are zero except for the 922-m record in 2014–15, and the 894-m record in 2015–16. For both of those deployments the deep current record lags the shallower records by 2 days. Divisions into three vertical groups are indicated at the left.

Fig. 9. The first two EOF modes of variability of the along-shelf flow (rotation of 310°) colored by deployment year. The time series were normalized by their respective standard deviations. (a) The fraction of the variance of each time series represented by the first EOF mode (EOF1). (b) The fraction of the variance of each time series represented by the second EOF mode (EOF2). Note that a negative fraction indicates negative correlations between the EOF mode and the time series and positive indicates a positive correlation.

Fig. 10. (a) Potential temperature–salinity diagram, with potential density contours in black, for the Chukchi Shelf and continental slope. Red lines indicate nominal water mass boundaries (after Corlett and Pickart, 2017), and include: melt water (MW), Alaskan Coastal Water (ACW), Bering Sea Water (BSW), Winter Water (WW), Remnant Winter Water (RWW) and Atlantic Water (AW). Hydrographic data from a summer 2017 cruise are shown (gray) for context, with data (45 m) at C9 in 2016–2017 (cyan). Three years of moored data near the core depth of the AW are colored by deployment year, which is expanded in (b). The mean (c) potential temperature and (d) salinity profiles near the C9 location from historical profiles are drawn in black; gray shading represents the standard deviation. The number of profiles used to construct the means is shown to the left of (c). The inset map shows the locations of: C9 (green); the 2017 cruise data (gray) used in (a) and (b); and the historical profiles (black) used to calculate (c) and (d).

Fig. 11. (a) Time series of salinity at 45 m (black) and the daily percent ice cover (blue) in a 50 km × 50 km box centered at C9. (b) Contours of temperature at the C9 mooring spanning 50–450

m depth from September 2016 to July 2017 (color). Depth of the 0° isotherm is overlaid (white contour). Instrument depths are indicated by the white bars at the left.

Fig. 12. (a) ERA5 winds at C9, and (b) contours of ocean temperature (color) and current velocity (vectors) at indicated depths during 15–31 October 2016. No ice was near C9 in October. (c) As in (a) during 13–31 December 2016, with percent ice cover indicated in blue. (d) As in (b) except for 13–31 December 2016. The currents are low pass filtered and rotated 310° (upward is approximately northwestward) and ice is percent cover in the 50 km × 50 km box centered on C9.

Fig. 13. Wavelet analysis for (a) along slope (rotated 310°), depth average (0–200 m) flow at C9, and (b) along-slope flow at ~240 m for October 2014 – July 2017. The blue-shaded contours are quartiles. Closed black contours denote peaks of significant energy. Areal sea-ice concentration (>85%) in a 50 km × 50 km box centered on C9 is indicated in green above (a). (c) Time series used to create (a) and (b) are shown.

Fig. 14. (a) Map of the Chukchi Sea with the location of the C9 mooring (black dot) and the regions over which wind and wind stress curl were averaged. (b) Histogram of hourly 10-m ERA5 wind averaged over the offshore rectangle encompassing C9 in (a). Wind blows toward the direction indicated. (c) Along- and across-slope components of 10-m ERA5 winds (rotated 310°). Values were averaged over the offshore box encompassing C9 as shown in (a) and low-pass filtered with a 15.5 day Hanning window. (d) Wind stress curl (gray) calculated from the hourly ERA5 winds averaged over the ellipse spanning the northeast Chukchi Sea in (a), and

low-pass filtered with a 15.5 day Hanning window (black). (e) Across slope difference of wind stress curl, as a proxy for an across slope sea-surface deformation, calculated from averages over the offshore and shelf boxes in (a). The hourly ERA5 data are gray and the 15.5-day Hanning window filtered time series is black. (f) ERA5 wind stress curl averaged over the Canada Basin as indicated by the large black circle in (a). Hourly values are gray and the 15.5-day Hanning window filtered values are black. (g) The upper 200 m depth average along-slope current measured by the C9 mooring (hourly values - gray, 15.5-day Hanning window filtered values - black).

Fig. 15. (a) Monthly depth-averaged (0–200 m) velocity at C9 versus transport at Icy Cape using only data when the mean velocity at C9 was positive (toward the northwest). Best fit line and associated r^2 value are shown. (b) Time series of the depth-averaged (0–200 m) monthly mean velocity at C9 (solid line; left axis) and the monthly mean transport at Icy Cape (dotted line; right axis). The vertical dashed lines represent the timing of the strong velocity events identified in (a).

References

Aagaard, K., Carmack, E., 1989. The role of sea ice and other fresh water in the Arctic circulation. J. Geophys. Res. 94, 14,485–14,498.

Armitage, T.W.K., Bacon, S., Ridout, A.L., Petty, A.A., Wolbach, S., Tsamados, M., 2017. Arctic Ocean surface geostrophic circulation 2003–2014. The Cryosphere 11, 1767–1780. https://doi.org/10.5194/tc-11-1767-2017.

Belmonte Rivas, M., and Stoffelen, A., 2019. Characterizing ERA-Interim and ERA5 surface wind biases using ASCAT. Ocean Sci. 15, 831–852, https://doi.org/10.5194/os-15-831-2019.

Bourke, R.H., Paquette, R.G., 1976. Atlantic water on the Chukchi Shelf. Geophys. Res. Lett. 3(10), 629–-632. https://doi.org/10.1029/GL003i010p00629.

Coachman, L.K., Aagaard, K., Tripp, R.B., 1975. Bering Strait: The Regional Physical Oceanography, Univ. of Washington Press, Seattle, Wash.

Corlett, W.B., Pickart, R.S., 2017. The Chukchi slope current. Prog. Oceanogr. 153, 50–65. https://doi.org/10.1016/j.pocean.2017.04.005.

Danielson, S. L., Weingartner, T.J., Hedstrom, K.S., Aagaard, K., Woodgate, R., Curchitser, E., Stabeno, P.J., 2014. Coupled wind-forced controls of the Bering-Chukchi Shelf circulation and the Bering Strait throughflow: Ekman transport, continental shelf waves, and variations of the Pacific-Arctic sea surface height gradient. Prog. Oceanogr. 125, 40–61. https://doi.org/10.1016/j.pocean.2014.04.006.

Dee, D.P., Uppala, S.M., Simmons, A.J., Berrisford, P., Poli, P., Kobayashi, S., Andrae, U., Balmaseda, M.A., Balsamo, G., Bauer, P., Bechtold, P., Beljaars, A.C.M., van de Berg, L., Bidlot, J., Bormann, N., Delsol, C., Dragani, R., Fuentes, M., Geer, A.J., Haimberger,

L., Healy, S.B., Hersbach, H., Hólm, E.V., Isaksen, L., Kållberg, P., Köhler, M., Matricardi, M., Mcnally, A.P., Monge-Sanz, B.M., Morcrette, J.J., Park, B.K., Peubey, C., de Rosnay, P., Tavolato, C., Thépaut, J.N., Vitart, F.,2011. The ERA-Interim reanalysis: configuration and performance of the data assimilation system. Q. J. Roy. Meteorol. Soc., 137, 553–597. https://doi.org/10.1002/qj.828.

Doddridge, E.W., Meneghello, G., Marshall, J., Scott, J., Lique, C., 2019. A Three-way balance in the Beaufort Gyre: The Ice-Ocean Governor, wind stress, and eddy diffusivity. J. Geophys. Res. Oceans 124, 3107–3124. https://doi.org/10.1029/2018JC014897.

Fine, E.C., MacKinnon, J.A., Alford, M.H., Mickett, J.B., 2018. Microstructure observations of turbulent heat fluxes in a warm-core Canada Basin eddy. J. Phys. Oceanogr., 48, 2397–2418, https://doi.org/10.1175/JPO-D-18-0028.1.

Giles, K.A., Laxon, S.W., Ridout, A.L., Wingham, D.J., Bacon, S., 2012. Western Arctic Ocean freshwater storage increased by wind-driven spin-up of the Beaufort Gyre. Nature Geoscience, 5, 194–197, https://doi.org/10.1038/ngeo1379.

Gong, D., Pickart, R.S., 2016. Early summer water mass transformation in the eastern Chukchi Sea. Deep Sea Res. Part II 130, 43–55. https://doi.org/10.1016/j.dsr2.2016.04.015.

Haiden, T., Janousek, M., Bidlot, J., Ferranti, L., Prates, F., Vitart, F., Bauer, P., Richardson, D.S., 2017. Evaluation of ECMWF forecasts, including 2016–2017 upgrades. European Centre for Medium-Range Weather Forecasts, ECMWF Tech. Memo. 817, 56 pp. https://doi.org/10.21957/x397za5p5.

Hersbach, H., de Rosnay, P., Bell, B., Schepers, D., Simmons, et al., 2018. Operational global reanalysis: progress, future directions and synergies with NWP. European Centre for Medium-Range Weather Forecasts, ERA Report Series, 27, 63 pp.

Itoh, M., Nishino, S., Kawaguchi, Y., Kikuchi, T., 2013. Barrow Canyon volume, heat, and freshwater fluxes revealed by long-term mooring observations between 2000 and 2008. J. Geophys. Res. Oceans 118(9), 4363–4379. https://doi.org/10.1002/jgrc.20290.

Jackson, J.M., Williams, W.J., Carmack, E.C., 2012. Winter sea-ice melt in the Canada Basin, Arctic Ocean. Geophys. Res. Lett., 39, L03603, https://doi.org/10.1029/2011GL050219.

Ladd, C., Mordy, C.W., Salo, S.A., Stabeno, P.J., 2016. Winter water properties and the Chukchi Polynya. J. Geophys. Res. Oceans 121, 5516–5534. https://doi.org/10.1002/2016JC011918.

Large, W.G., Pond, S., 1981. Open ocean momentum flux measurements in moderate to strong winds. J. Phys. Oceanogr. 11, 324–336.

Li, M., Pickart, R.S., Spall, M.A., Weingartner, T.J., Lin, P., Moore, G., Qi, Y., 2019. Circulation of the Chukchi Sea shelfbreak and slope from moored timeseries. Prog. Oceanogr. 172, 14–33. https://doi.org/10.1016/j.pocean.2019.01.002.

Linders, J., Pickart, R.S., Björk, G., Moore, G.W.K., 2017. On the nature and origin of water masses in Herald Canyon, Chukchi Sea: Synoptic surveys in summer 2004, 2008, and 2009. Prog. Oceanogr., 159, 99–114. https://doi.org/10.1016/j.pocean.2017.09.005.

Lindsay, R., Wensnahan, M., Schweiger, A., and Zhang, J., 2014. Evaluation of seven different atmospheric reanalysis products in the Arctic. J. Climate 27, 2588–2606, https://doi.org/10.1175/JCLI-D-13-00014.1.

Mesinger, F., DiMego, G., Kalnay, E., Mitchell, K., Shafran, P.C., Ebisuzaki, W., Jovic, D., Woollen, J., Rogers, E., Berbery, E.H., Ek, M.B., Fan, Y., Grumbine, R., Higgins, W., Li, H., Lin, Y., Manikin, G., Parrish, D., Shi, W., 2006. North American Regional

Reanalysis. Bull. Am. Meteorol. Soc. 87, 343–360. https://doi.org/10.1175/BAMS-87-3-343.

Moore, G.W.K., 2012. Decadal variability and a recent amplification of the summer Beaufort Sea High. Geophys. Res. Lett, 39, L10807, https://doi.org/10.1029/2012GL051570.

Moore, G.W.K., Pickart, R.S., Renfrew, I.A., 2008. Buoy observations from the windiest location in the world ocean, Cape Farewell, Greenland. Geophys. Res. Lett. 35, L18802. https://doi.org/10.1029/2008GL034845.

Nikolopoulos, A., Pickart, R.S., Fratantoni, P.S., Shimada, K., Torres, D.J., Jones, E.P., 2009. The western Arctic boundary current at 152 W: Structure, variability, and transport. Deep-Sea Res. Part II 56, 1164–1181. https://doi.org/10.1016/j.dsr2.2008.10.014.

Peralta-Ferriz, C., Woodgate, R.A., 2017. The dominant role of the East Siberian Sea in driving the oceanic flow through the Bering Strait—Conclusions from GRACE ocean mass satellite data and in situ mooring observations between 2002 and 2016. Geophys. Res. Lett. 44, 11,472–11,481. https://doi.org/10.1002/2017GL075179.

Petty, A.A., Hutchings, J.K., Richter-Menge, J.A., Tschudi, M.A., 2016. Sea ice circulation around the Beaufort Gyre: The changing role of wind forcing and the sea ice state. J. Geophys. Res. Oceans 121(5), 3278–3296. doi:10.1002/2015JC010903.

Pickart, R.S., Pratt, L.J., Torres, D.J., Whitledge, T.E., Proshutinsky, A.Y., Aagaard, K., Agnew, T.A., Moore, G. W. K., Dail, H.J., 2010. Evolution and dynamics of the flow through Herald Canyon in the western Chukchi Sea. Deep-Sea Res. Part II 57(1–2), 5–26. https://doi.org/10.1016/ j.dsr2.2009.08.002.

Pisareva, M.N., Pickart, R.S., Lin, P., Fratantoni, P.S., Weingartner, T.J., 2019. On the nature of wind-forced upwelling in Barrow Canyon. Deep-Sea Res. II, 162, 63–78, https://doi.org/10.1016/ j.dsr2.2019.02.002.

Polyakov, I.V., Pnyushkov, A.V., Alkire, M.B., Ashik, I.M., Baumann, T.M., 2017. Greater role for Atlantic inflows on sea-ice loss in the Eurasian Basin of the Arctic Ocean. Science 356(6335), 285–291. https://doi.org/10.1126/science.aai8204.

Proshutinsky, A., Krishfield, R., Timmermans, M.-L., 2019. Preface to special issue Forum for Arctic Ocean Modeling and Observational Synthesis (FAMOS) 2: Beaufort Gyre phenomenon. J. Geophys. Res. Oceans, *in press*. https://doi.org/10.1029/2019JC015400.

Regan, H.C., Lique, C., Armitage, T.W.K., 2019. The Beaufort Gyre extent, shape, and location between 2003 and 2014 from satellite observations. J. Geophys. Res. Oceans 124, 844–862. https://doi.org/10.1029/2018JC014379.

Renfrew, I.A., Peterson, G.N., Sproson, D.A.J., Moore, G.W.K., Adiwidjaja, H., Zhang, S., North, R., 2009. A comparison of aircraft-based surface-layer observations over Denmark Strait and the Irminger Sea with meteorological analyses and QuikSCAT winds. Q. J. R. Meteorol. Soc. 135, 2046–2066. https://doi.org/10.1002/qj.444.

Serreze, M.C., Crawford, A.D., Stroeve, J.C., Barrett, A.P., Woodgate, R.A., 2016. Variability, trends, and predictability of seasonal sea ice retreat and advance in the Chukchi Sea. J. Geophys. Res. Oceans, 121, 7308–7325, https://doi.org/10.1002/2016JC011977.

Shimada, K., Carmack, E.C., Hatakeyama, K., Takizawa, T., 2001. Varieties of shallow temperature maximum waters in the western Canada Basin of the Arctic Ocean. Geophys. Res. Lett., 28, 3441–3444.

Spall, M., Pickart, R., Li, M., Itoh, M., Lin, P., Kikuchi, T., Qi, Y., 2018. Transport of Pacific

water into the Canada Basin and the formation of the Chukchi Slope Current. J. Geophys. Res. Oceans 123, 7453–7471. https://doi.org/10.1029/2018JC013825.

Stabeno, P., Kachel, N., Ladd, C., Woodgate, R., 2018. Flow patterns in the eastern Chukchi Sea: 2010–2015. J. Geophys. Res. Oceans 123, 1177–1195. https://doi.org/10.1002/2017JC013135.

Stabeno, P.J., Bell, S., Cheng, W., Danielson, S., Kachel, N.B., Mordy, C.W., 2016a. Long-term observations of Alaska Coastal Current in the northern Gulf of Alaska. *Deep-Sea Res. II*, *132*, 24–40, doi: 10.1016/j.dsr2.2015.12.016, Understanding Ecosystem Processes in the Gulf of Alaska: Volume 1.

Stabeno, P.J., Danielson, S.L., Kachel, D.G., Kachel, N.B., Mordy, C.W., 2016b. Currents and transport on the Eastern Bering Sea shelf: An integration of over 20 years of data. *Deep-Sea Res. II*, *134*, 13-29, https://doi.org/10.1016/j.dsr2.2016.05.010

Stabeno, P.J., N.A. Bond, A.J. Hermann, N.B. Kachel, C.W. Mordy, and J.E. Overland (2004): Meteorology and oceanography of the northern Gulf of Alaska. *Cont. Shelf Res.*, *24*, 859–897, doi: 10.1016/j.csr.2004.02.007.

Stabeno, P.J.,R.K. ReedCirculation in the Bering Sea basin observed by satellite-tracked drifters: 1986–1993 J. Phys. Oceanogr., 24 (4) (1994), pp. 848-854

Steele, M., Morison, J., Ermold, W., Rigor, I., Ortmeyer, M., Shimada, K., 2004. Circulation of summer Pacific halocline water in the Arctic Ocean. J. Geophys. Res., 109, C02027, https://doi.org/10.1029/2003JC002009.

Steele, M., Ermold, W., Zhang, J., 2008. Arctic Ocean surface warming trends over the past 100 years. Geophys. Res. Lett., 35, L02614, https://doi.org/10.1029/2007GL031651.

Stegall, S.T., Zhang, J., 2012. Wind field climatology, changes, and extremes in the Chukchi-Beaufort Seas and Alaska North Slope during 1979–2009. J. Clim. 25, 8075–8089. https://doi.org/10.1175/JCLI-D-11-00532.1.

Timmermans, M.-L., Proshutinsky, A., Golubeva, E., Jackson, J.M., Krishfield, R., McCall, M., Platov, G., Toole, J., Williams, W., Kikuchi, T., and Nishino, S., 2014. Mechanisms of Pacific Summer Water variability in the Arctic central Canada Basin. J. Geophys. Res. Oceans, 119, 7523–7548, https://doi.org/10.1002/2014JC010273.

Timmermans, M.-L., 2015. The impact of stored solar heat on Arctic sea ice growth. Geophys. Res. Lett., 42, 6399 – 6406, https://doi.org/10.10022015GL064541.

Timmermans, M.-L., Toole, J., Krishfield, R., 2018. Warming of the interior Arctic Ocean linked to sea ice losses at the basin margins. Science Advances, 4(8), eaat6773, https://doi.org/10.1126/sciadv.aat6773.

Torrence, C., Compo, G.P., 1998. A practical guide to wavelet analysis. Bull. Am. Meteorol. Soc. 79, 61–78. https://doi.org/10.1175/1520-0477(1998)079<0061:APGTWA>2.0.CO;2.

Tsukada, Y., Ueno, H., Ohta, N., Itoh, M., Watanabe, E., Kikuchi, T., Nishino, S., Mizobata, K., 2018. Interannual variation in solar heating in the Chukchi Sea, Arctic Ocean. Polar Science, 17, 33–39, https://doi.org/10.1016/j.polar.2018.06.003.

Watanabe, E., Onodera, J., Itoh, M., Nishino, S., Kikuchi, T., 2017. Winter transport of subsurface warm water toward the Arctic Chukchi Borderland. Deep-Sea Res. I, 128, 115–130, https://doi.org/10.1016/j.dsr.2017.08.009.

Weingartner, T., Aagaard, K., Woodgate, R., Danielson, S., Sasaki, Y., Cavalieri, D., 2005. Circulation on the north central Chukchi Sea shelf. Deep-Sea Res. Part II 52(24–26), 3150–3174. https://doi.org/10.1016/j.dsr2.2005.10.015.

Wood, K.R., Jayne, S.R., Mordy, C.W., Bond, N., Overland, J.E., Ladd, C., Stabeno, P.J., Ekholm, A.K., Robbins, P.E., Schreck, M., Heim, R., Intrieri, J., 2018. Results of the first Arctic Heat Open Science Experiment. Bull. Am. Meteorol. Soc. 99, 513–520. https://doi.org/10.1175/BAMS-D-16-0323.1.

Woodgate, R.A., Aagaard, K., Weingartner, T.J., 2005a. Monthly temperature, salinity, and transport variability of the Bering Strait through flow. Geophys. Res. Lett. 32, L04601. https://doi.org/10.1029/2004GL021880.

Woodgate, R.A., Aagaard, K., Weingartner, T.J., 2005b. A year in the physical oceanography of the Chukchi Sea: Moored measurements from autumn 1990–1991. Deep-Sea Res. Part II 52(24–26), 3116–3149. https://doi.org/10.1016/j.dsr2.2005.10.016.

Woodgate, R.A., Weingartner, T.J., Lindsay, R., 2012. Observed increases in Bering Strait oceanic fluxes from the Pacific to the Arctic from 2001 to 2011 and their impacts on the Arctic Ocean water column. Geophys. Res. Lett. 39, L24603. https://doi.org/10.1029/2012GL054092.

Woodgate, R.A., Aagaard, K., Muench, R.D., Gunn, J., Bjork, G., Rudels, B., Roach, A.T., Schauer, U., 2001. The Arctic Ocean boundary current along the Eurasian slope and the adjacent Lomonosov Ridge: Water mass properties, transports and transformations from moored instruments. Deep-Sea Res. Part I 48(8), 1757–1792.

Yang, J., Proshutinsky, A., Lin, X., 2016. Dynamics of an idealized Beaufort Gyre: 1. The effect of a small beta and lack of western boundaries. J. Geophys. Res. Oceans 121, 1249–1261. https://doi.org/10.1002/2015JC011296.

Zhang, J., Steele, M., Runciman, K., Dewey, S., Morison, J., Lee, C., Rainville, L., Cole, S., Krishfield, R., Timmermans, M., Toole, J., 2016. The Beaufort Gyre intensification and stabilization: A model-observation synthesis. J. Geophys. Res. Oceans 121, 7933–7952. https://doi.org/10.1002/2016JC012196.

Figures:

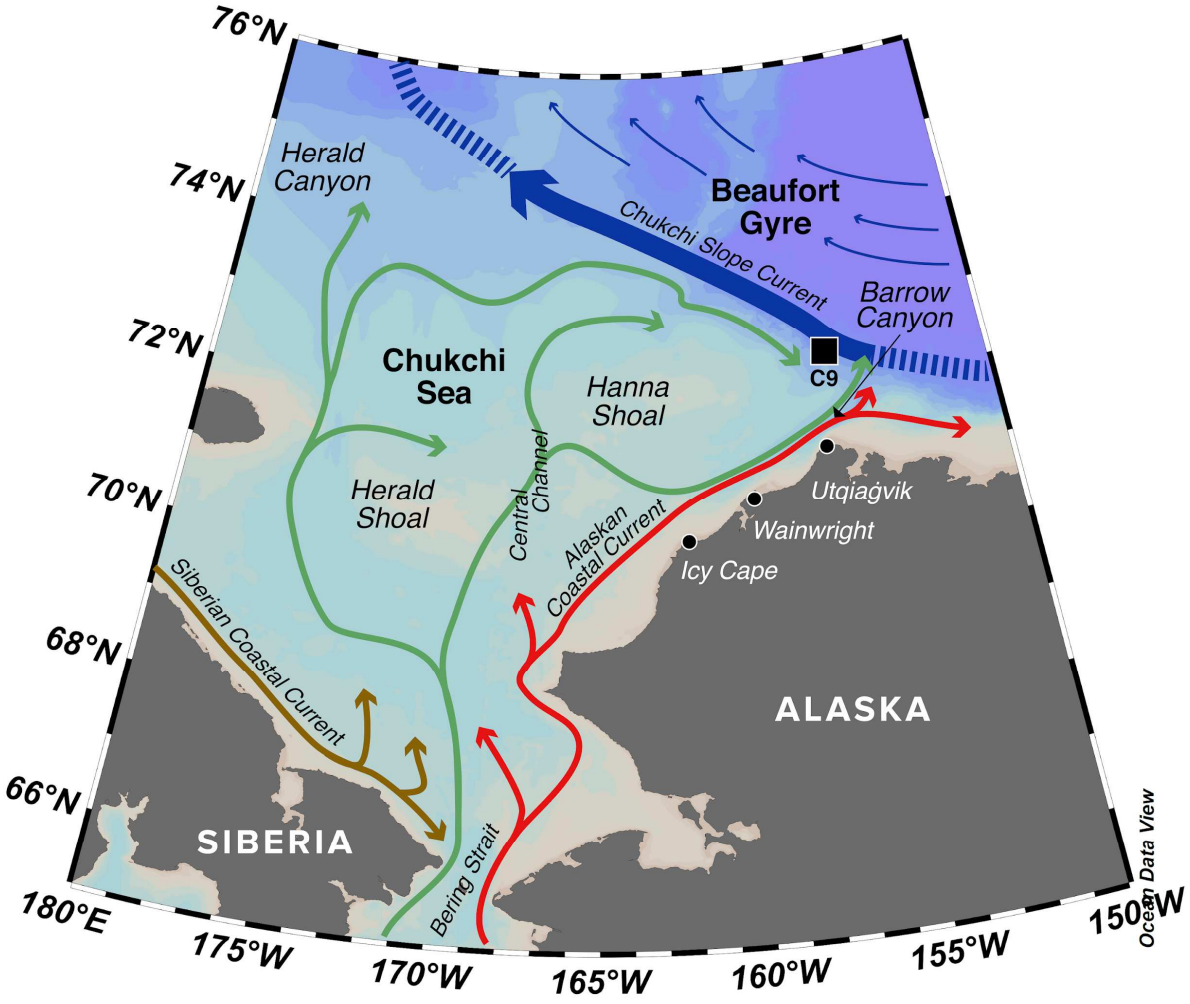

Fig. 1: Schematic map of surface flow patterns over the Chukchi Sea continental shelf and slope (adapted from Stabeno et al., 2018). The location of the C9 mooring, near the 1000-m isobath, is indicated with the black square.

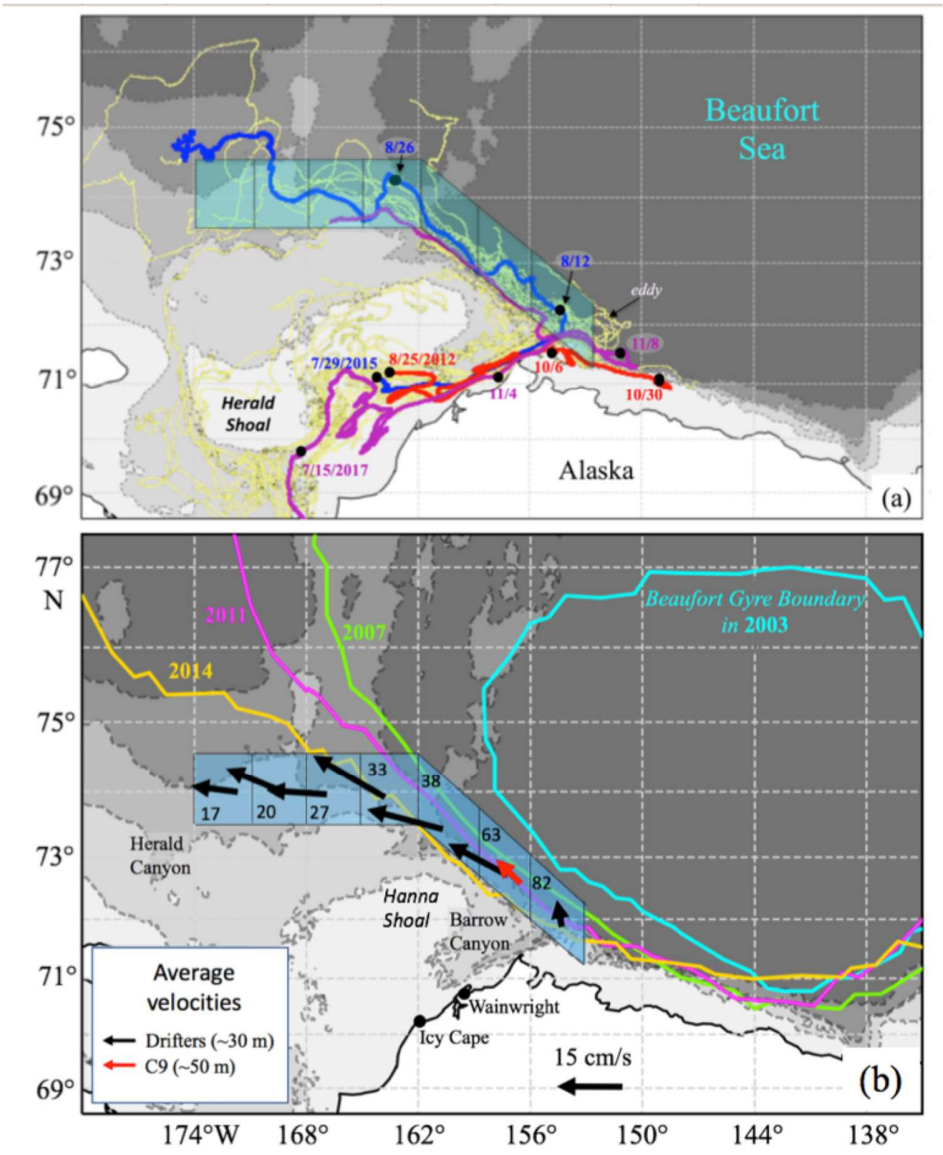

Fig. 2. (a) Drifter trajectories (drogue depth ~30 m). The yellow trajectories indicate drifters deployed in the region. Three individual drifter tracks, representative of three primary pathways, are shown in different colors: (1) eastward flow on the Beaufort Shelf (red); (2) first eastward flow and then northwestward flow (magenta); and (3) northwestward flow upon exiting Barrow Canyon (blue). Selected dates are indicated along each trajectory. (b) The position of the edge of the Beaufort Gyre during four different years (adapted from Regan et al., 2019, their Fig. 3). The mean Lagrangian velocity of the drifters in each box (black arrows), with the number of independent estimates that contributed to the mean (black numerals). The red arrow is the mean velocity at ~50 m from the three C9 mooring deployments.

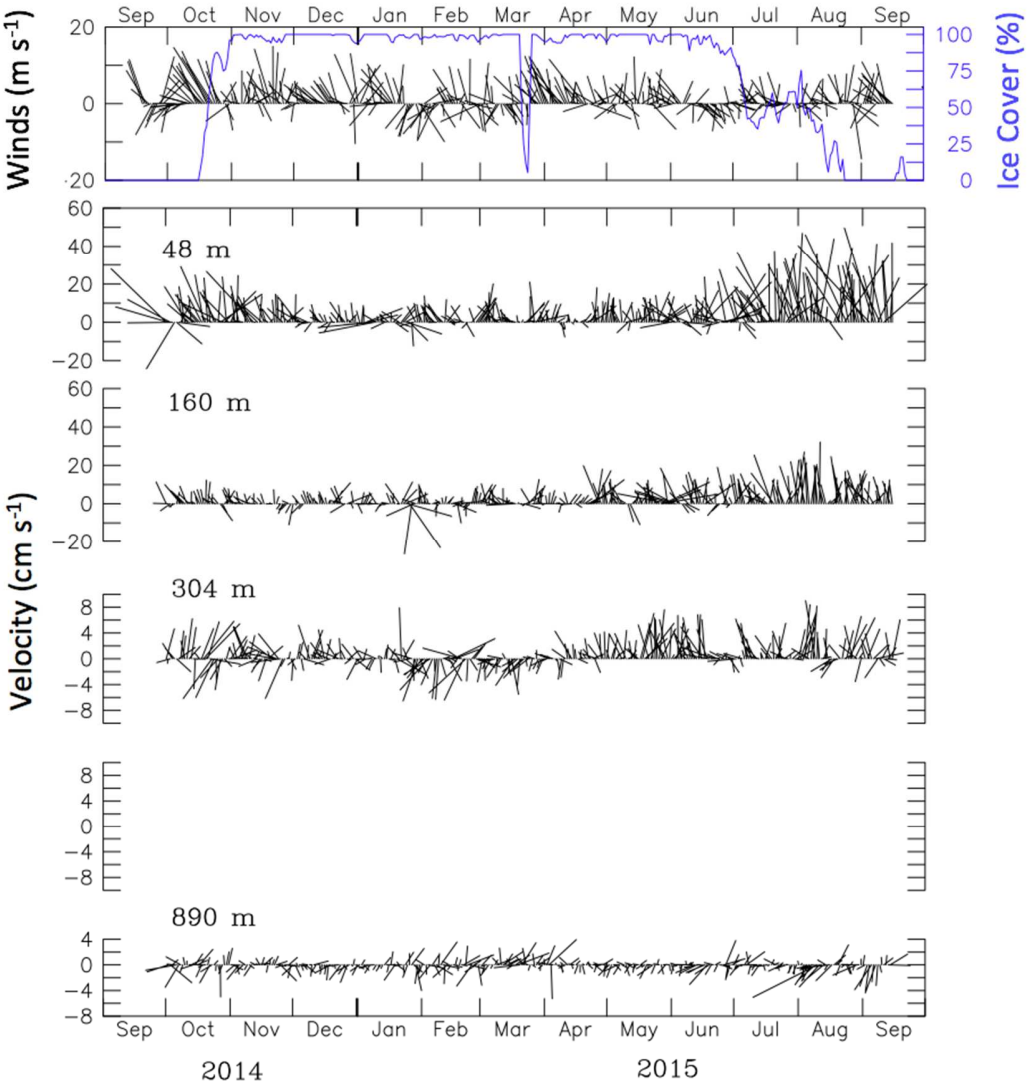

Fig. 3. (top panel) Daily ERA5 wind vectors interpolated onto the C9 mooring location and percent areal ice cover (blue) in a ~50 km × 50 km box centered on C9. (bottom panel) Low-pass filtered current velocities (daily) measured at C9 spanning September 2014 – September 2015. The depths of each time series of currents are indicated. Both the wind and velocity axes were rotated 310° so that upward is approximately northwestward along the continental slope. Note the different velocity scales.

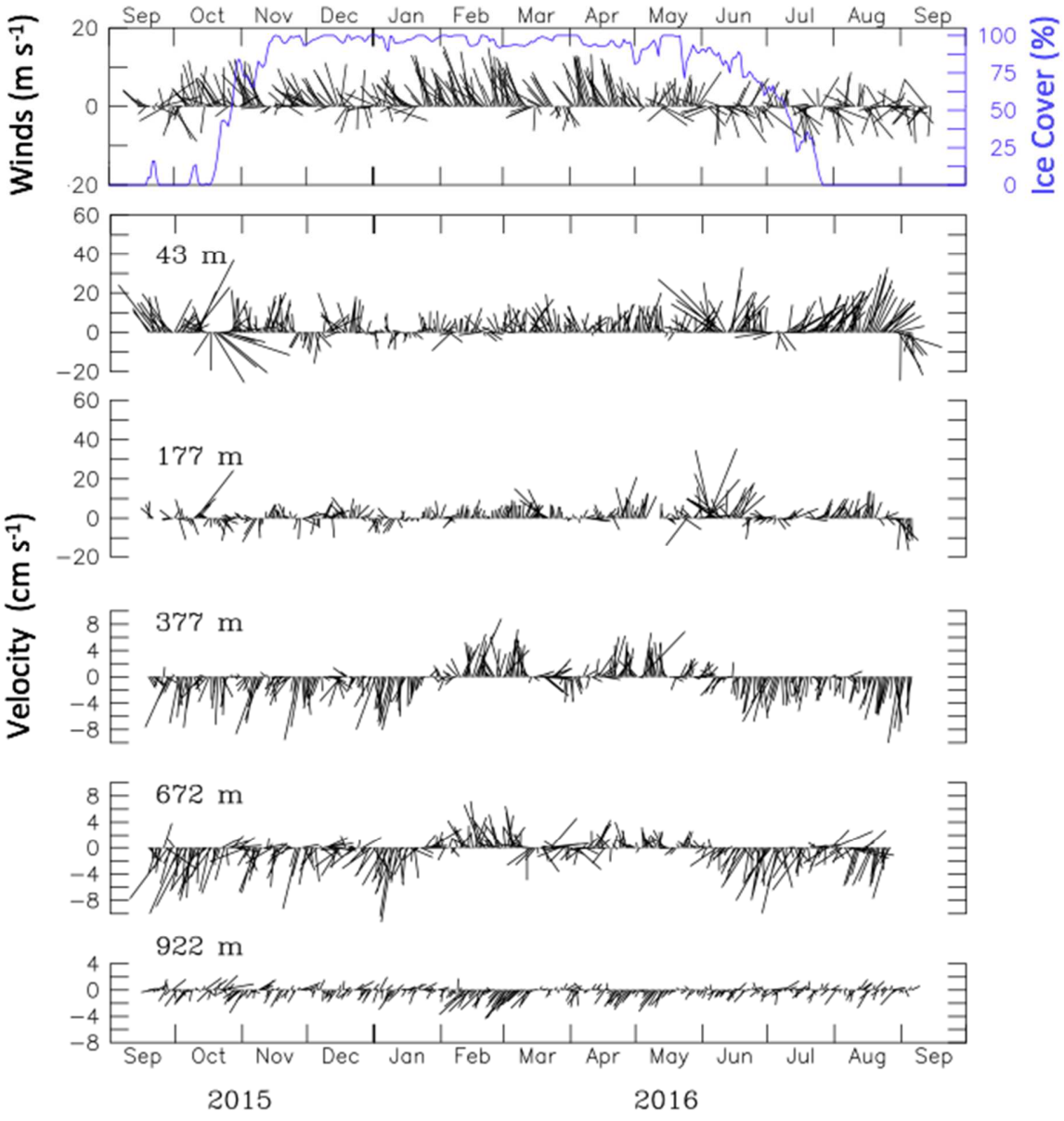

Figure 4. Same as Figure 3 except for September 2015 – September 2016.

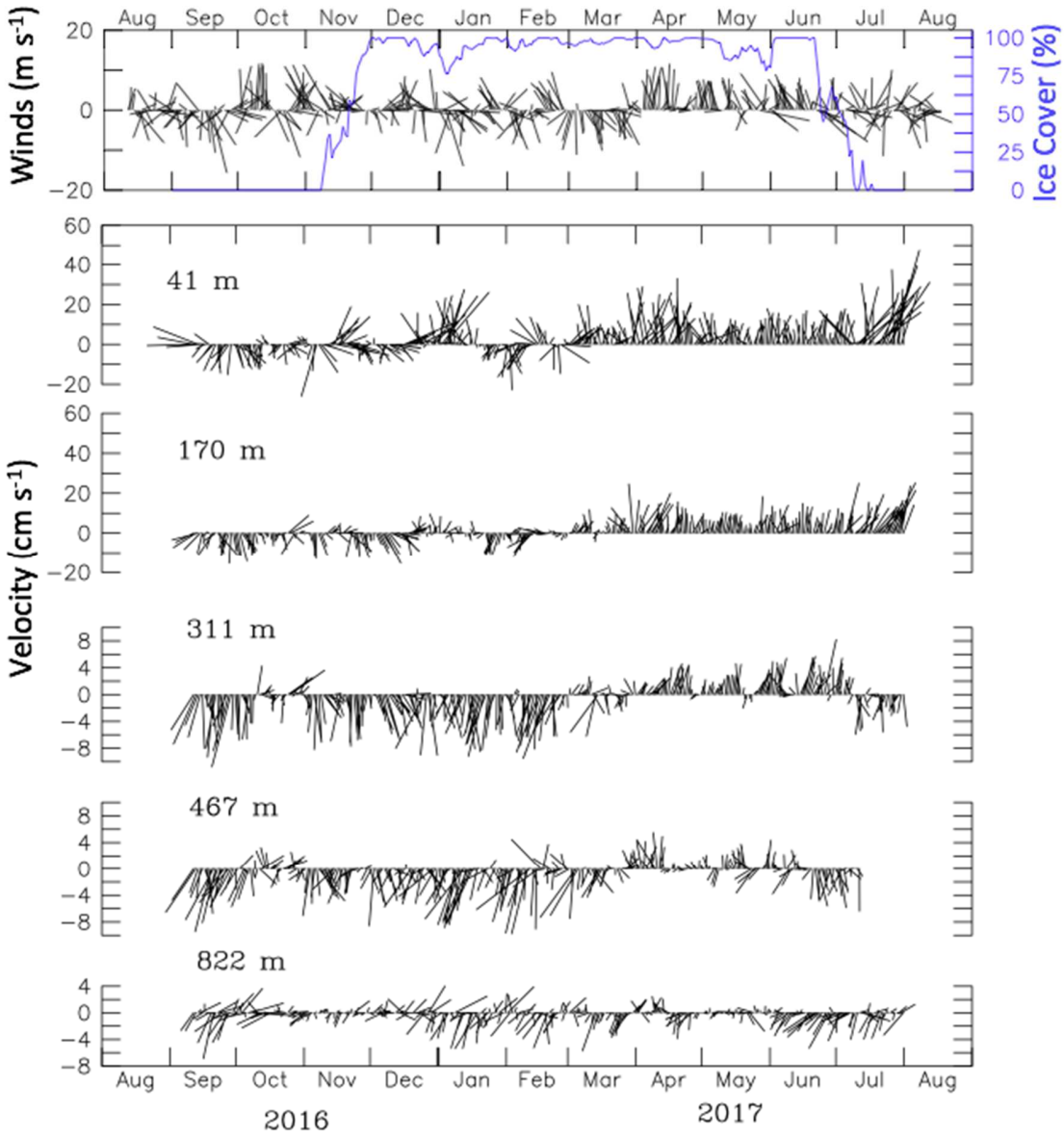

Figure 5. Same as Figure 3 except for September 2016 – August 2017.

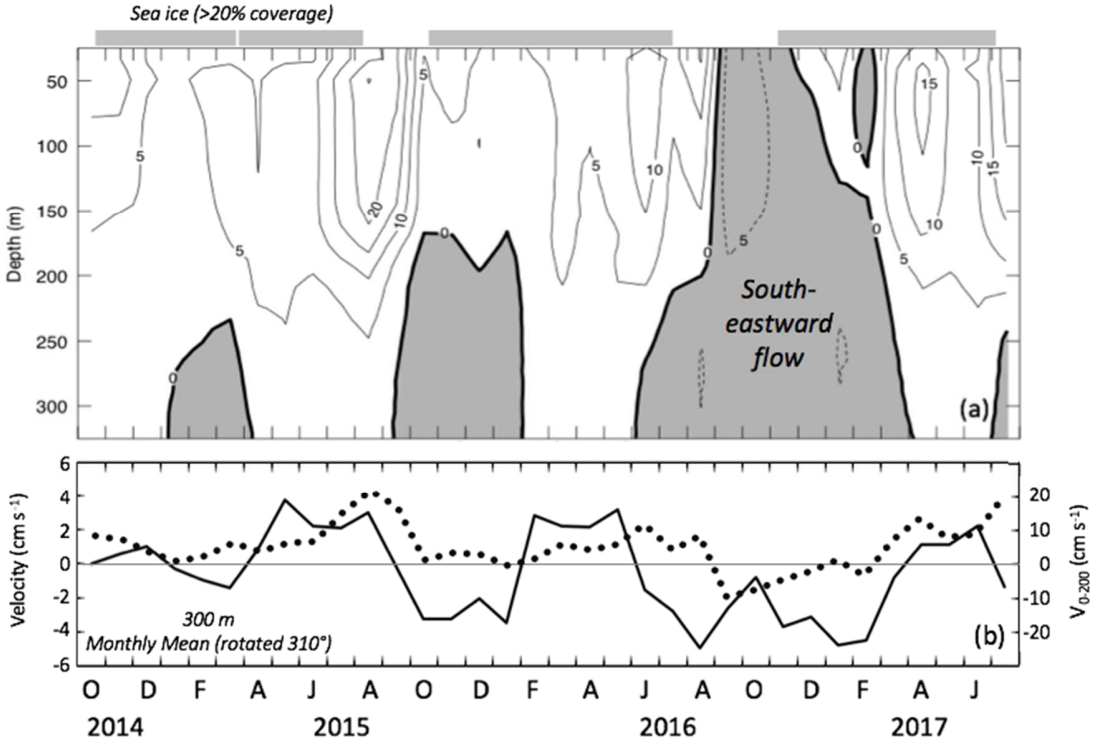

Figure 6. (a) Contours of monthly mean currents (rotated 310°) measured by the three ADCPs deployed at C9. Positive is approximately northwestward. At the top is the areal sea-ice cover (>20%) in the vicinity of C9. The shaded region represents negative (nominally southeastward) flow. (b) Monthly mean currents at ~300 m (solid line) and depth-averaged velocity, $V_{0\text{-}200}$, in the upper 200 m (dotted line). Positive is northwestward.

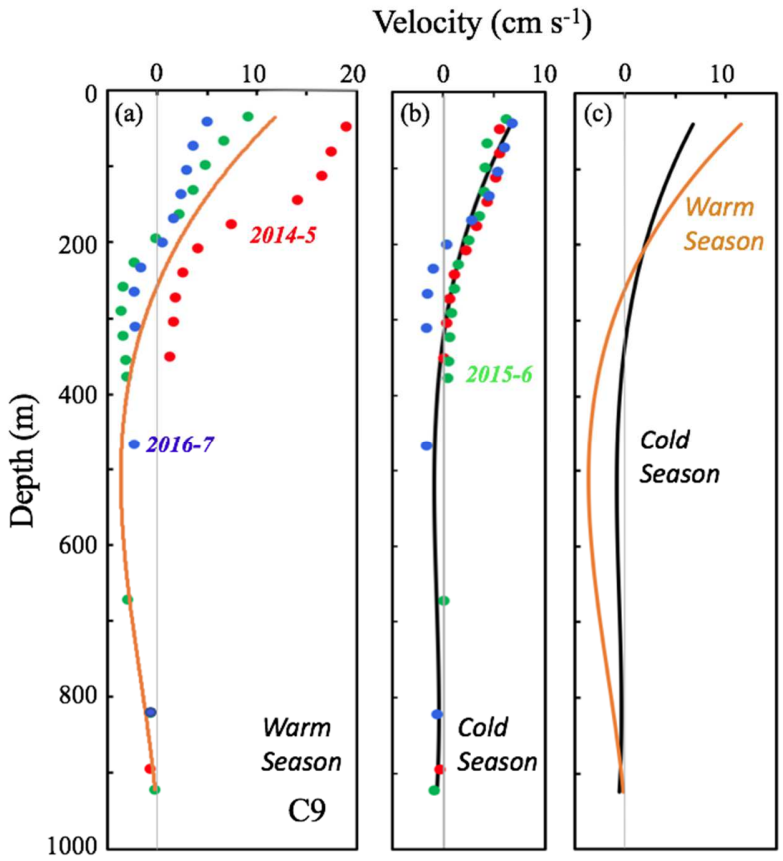

Figure 7. Mean alongshore flow in (a) the warm season, 1 July – 31 October, and (b) the cold season, 1 December – 31 May. Positive is approximately northwestward (310°). Colored dots represent averages for different deployment years (2014 is red, 2015 is green, 2016 is blue). Solid lines in (a) and (b) represent 3-year seasonal means and are least squares fits of a third-degree polynomial. (c) The 3-year seasonal means are shown separately to facilitate comparison.

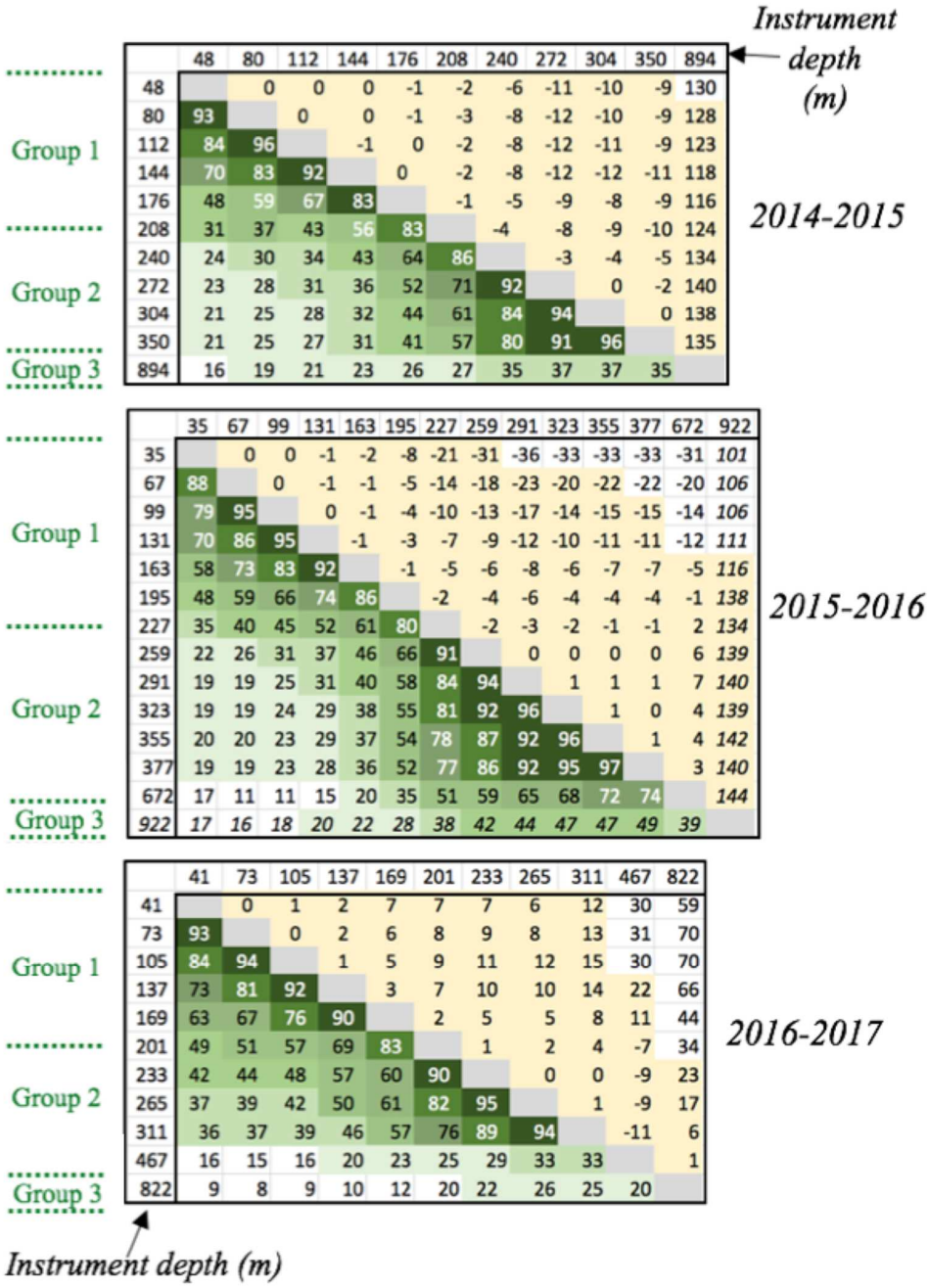

Figure 8. Complex correlations (below diagonal) and correlation angles (above diagonal) for currents for each of the three mooring deployments: (top) 2014 with 1350 data points; (middle) 2015 with 1372 data points; and (bottom) 2016 with 1200 data points. Instrument depths are in meters. The correlations are color coded from dark (high) to light (low) correlations. Shaded correlations are significant at $p<0.01$. All lags are zero except for the 922-m record in 2014–15, and the 894-m record in 2015–16. For both of those deployments the deep current record lags the shallower records by 2 days. Divisions into three vertical groups are indicated at the left.

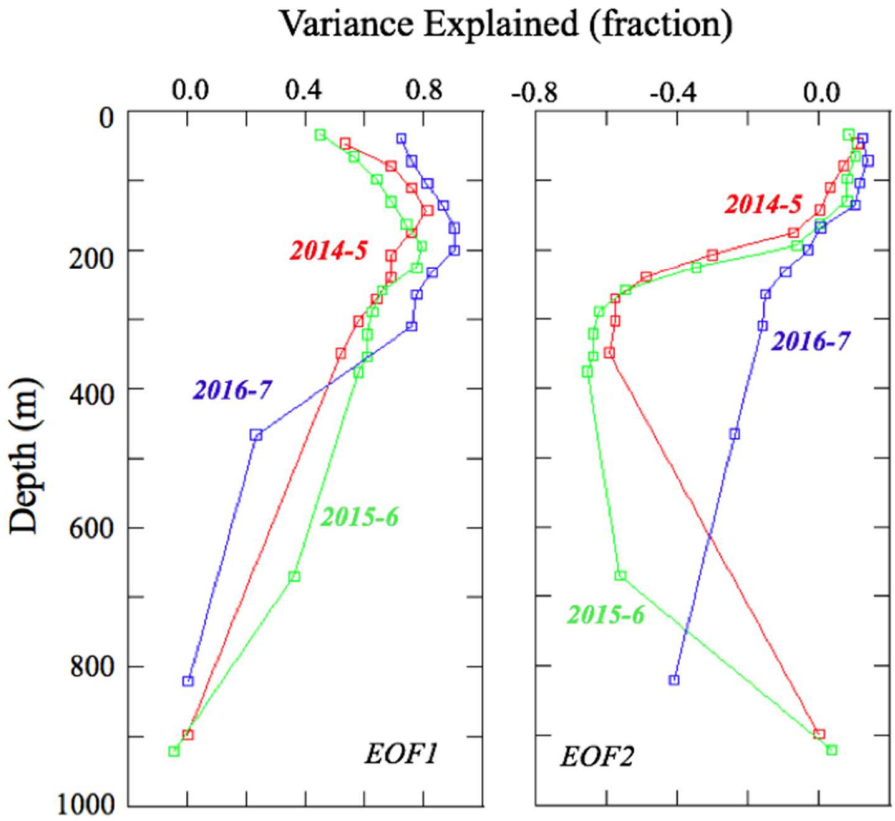

Figure 9. The first two EOF modes of variability of the along-shelf flow (rotation of 310°) colored by deployment year. The time series were normalized by their respective standard deviations. (left) The fraction of the variance of each time series represented by the first EOF mode (EOF1). (right) The fraction of the variance of each time series represented by the second EOF mode (EOF2). Note that a negative fraction indicates negative correlations between the EOF mode and the time series and positive indicates a positive correlation.

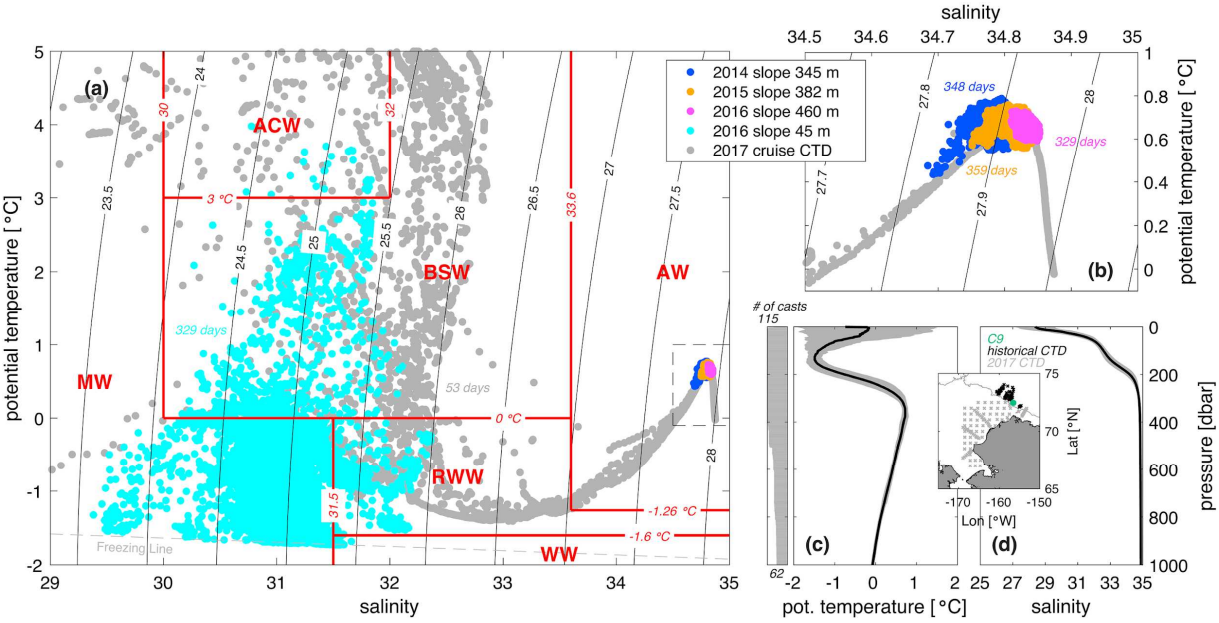

Figure 10. (a) Potential temperature–salinity diagram, with potential density contours in black, for the Chukchi Shelf and continental slope. Red lines indicate nominal water mass boundaries (after Corlett and Pickart, 2017), and include: melt water (MW), Alaskan Coastal Water (ACW), Bering Sea Water (BSW), Winter Water (WW), Remnant Winter Water (RWW) and Atlantic Water (AW). Hydrographic data from a summer 2017 cruise are shown (gray) for context, with data (45 m) at C9 in 2016–2017 (cyan). Three years of moored data near the core depth of the AW are colored by deployment year, which is expanded in (b). The mean (c) potential temperature and (d) salinity profiles near the C9 location from historical profiles are drawn in black; gray shading represents the standard deviation. The number of profiles used to construct the means is shown to the left of (c). The inset map shows the locations of: C9 (green); the 2017 cruise data (gray) used in (a) and (b); and the historical profiles (black) used to calculate (c) and (d).

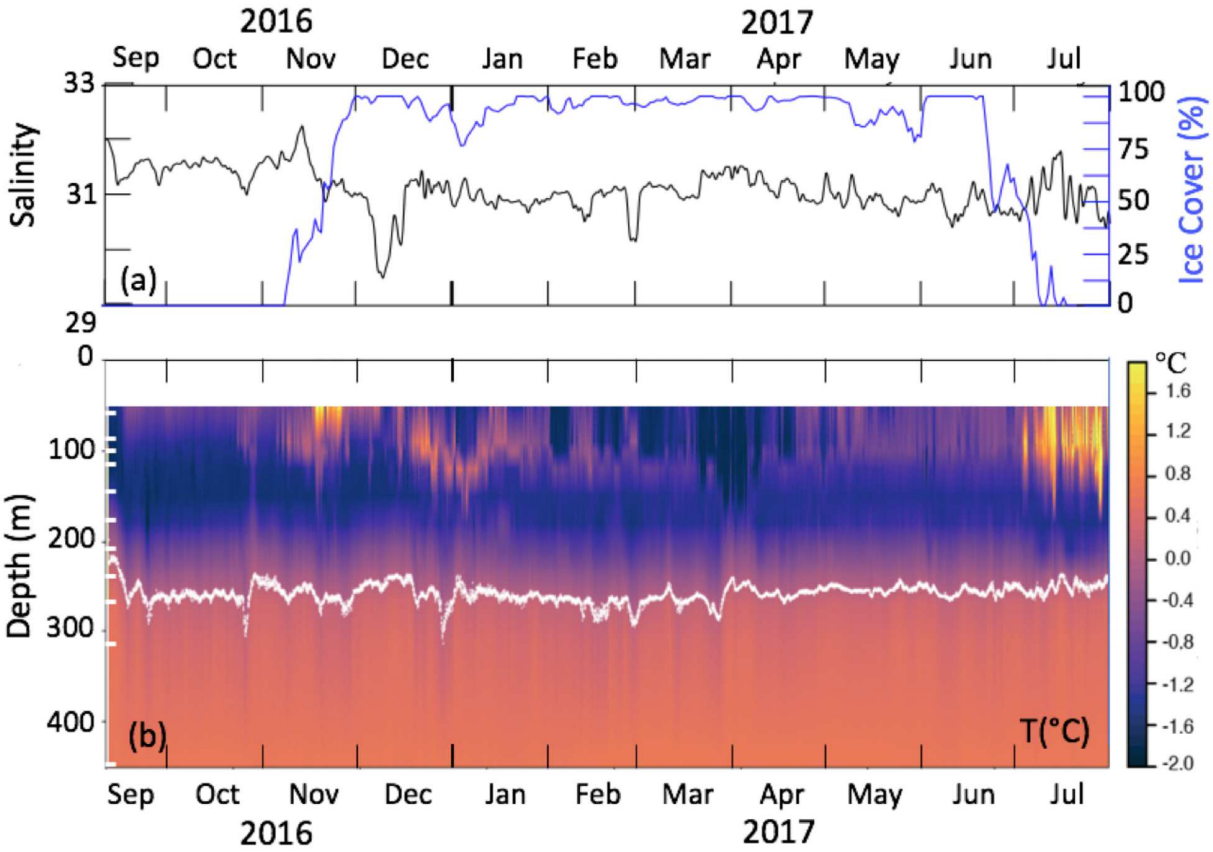

Figure 11. (a) Time series of salinity at 45 m (black) and the daily percent ice cover (blue) in a 50 km × 50 km box centered at C9. (b) Contours of temperature at the C9 mooring spanning 50–450 m depth from September 2016 to July 2017 (color). Depth of the 0° isotherm is overlaid (white contour). Instrument depths are indicated by the white bars at the left.

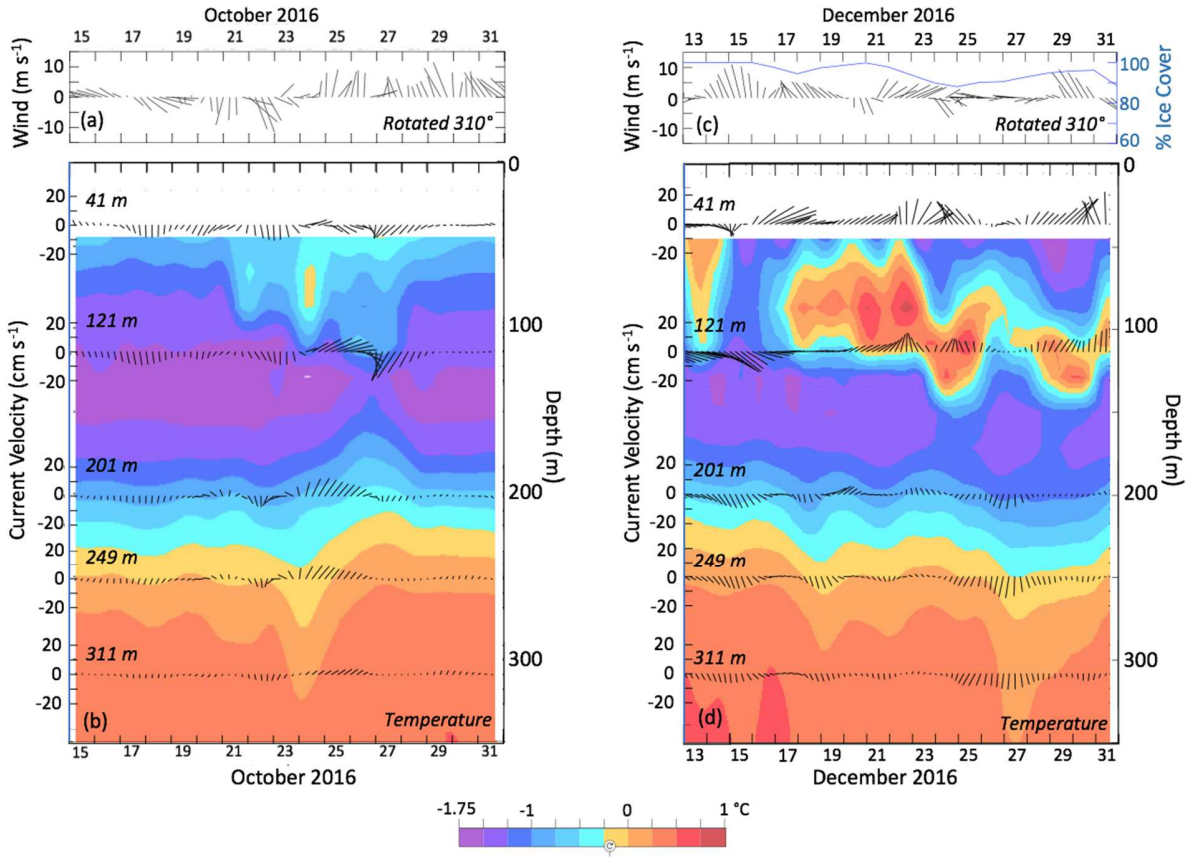

Figure 12. (a) ERA5 winds at C9, and (b) contours of ocean temperature (color) and current velocity (vectors) at indicated depths during 15–31 October 2016. No ice was near C9 in October. (c) As in (a) during 13–31 December 2016, with percent ice cover indicated in blue. (d) As in (b) except for 13–31 December 2016. The currents are low pass filtered and rotated 310° (upward is approximately northwestward) and ice is percent cover in the 50 km × 50 km box centered on C9.

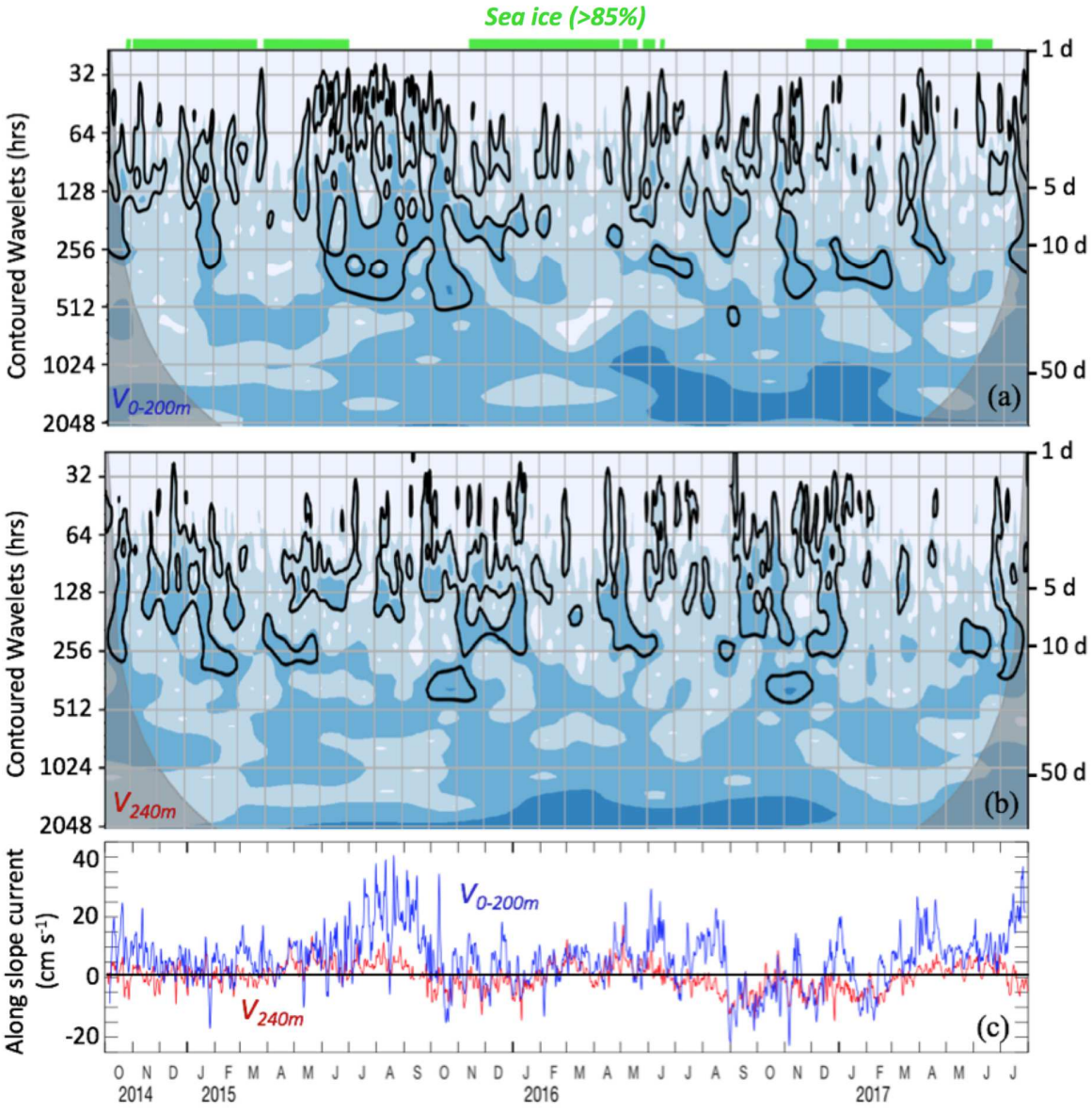

Figure 13. Wavelet analysis for (a) along slope (rotated 310°), depth average (0–200 m) flow at C9, and (b) along-slope flow at ~240 m for October 2014 – July 2017. The blue-shaded contours are quartiles. Closed black contours denote peaks of significant energy. Areal sea-ice concentration (>85%) in a 50 km × 50 km box centered on C9 is indicated in green above (a). (c) Time series used to create (a) and (b) are shown.

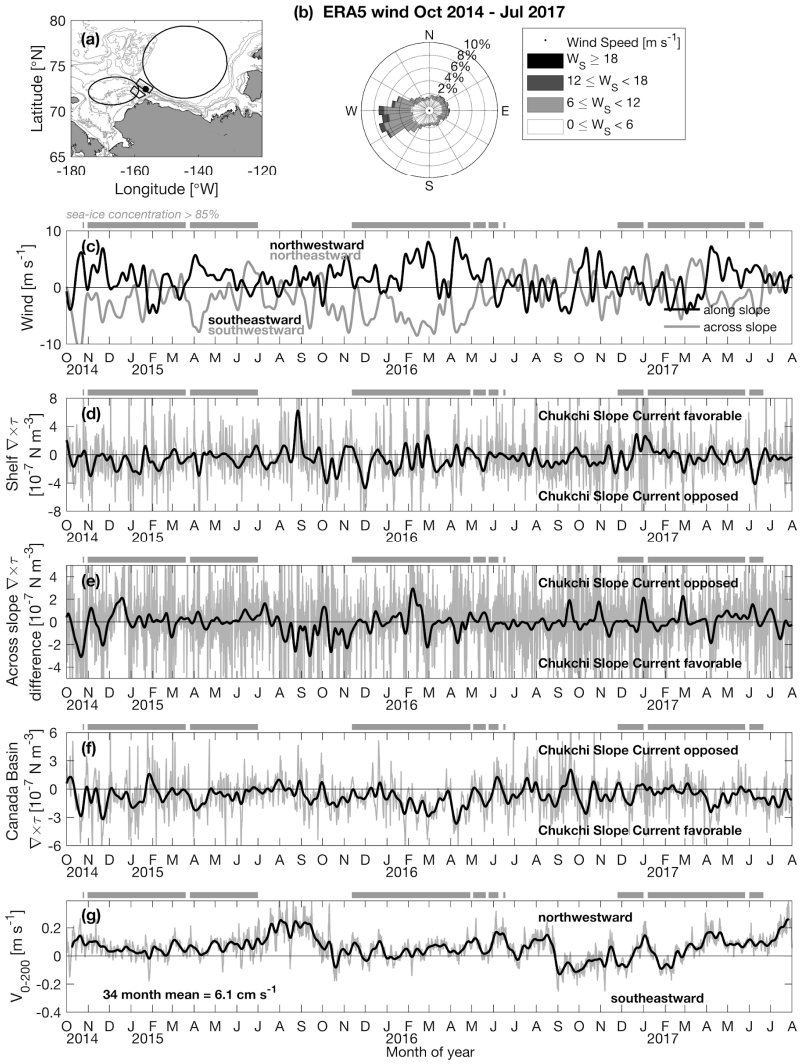

Figure 14. (a) Map of the Chukchi Sea with the location of the C9 mooring (black dot) and the regions over which wind and wind stress curl were averaged. (b) Histogram of hourly 10-m ERA5 wind averaged over the offshore rectangle encompassing C9 in (a). Wind blows toward the direction indicated. (c) Along- and across-slope components of 10-m ERA5 winds (rotated 310°). Values were averaged over the offshore box encompassing C9 as shown in (a) and low-pass filtered with a 15.5 day Hanning window. (d) Wind stress curl (gray) calculated from the hourly ERA5 winds averaged over the ellipse spanning the northeast Chukchi Sea in (a), and low-pass filtered with a 15.5 day Hanning window (black). (e) Across slope difference of wind stress curl, as a proxy for an across slope sea-surface deformation, calculated from averages over the offshore and shelf boxes in (a). The hourly ERA5 data are gray and the 15.5-day Hanning window filtered time series is black. (f) ERA5 wind stress curl averaged over the Canada Basin as indicated by the large black circle in (a). Hourly values are gray and the 15.5-day Hanning window filtered values are black. (g) The upper 200 m depth average along-slope current measured by the C9 mooring (hourly values - gray, 15.5-day Hanning window filtered values - black).

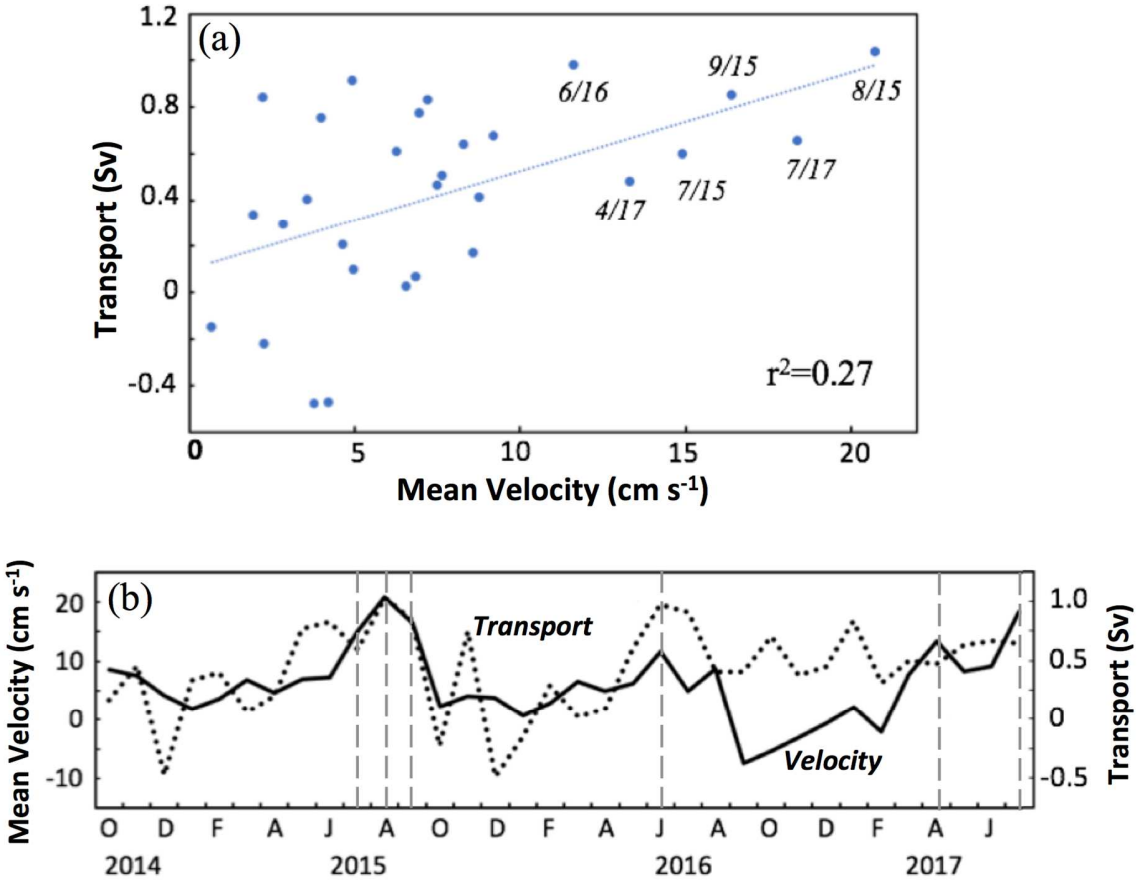

Figure 15. (a) Monthly depth-averaged (0–200 m) velocity at C9 versus transport at Icy Cape using only data when the mean velocity at C9 was positive (toward the northwest). Best fit line and associated r^2 value are shown. (b) Time series of the depth-averaged (0–200 m) monthly mean velocity at C9 (solid line; left axis) and the monthly mean transport at Icy Cape (dotted line; right axis). The vertical dashed lines represent the timing of the strong velocity events identified in (a).